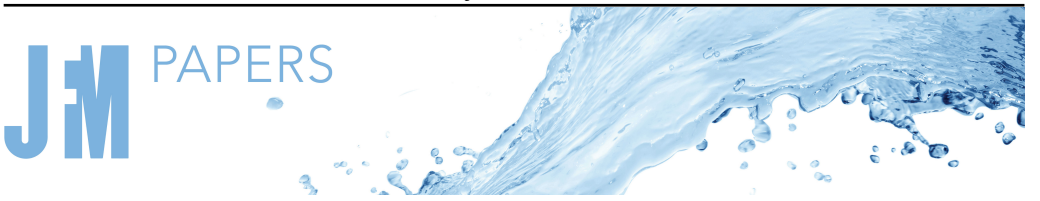
J. Fluid Mech. (2026), *vol.* 1031, A28, doi:10.1017/jfm.2026.11338



A numerical study on mass transfer in buoyancy-driven bubbly flows

Sanjid S. Chirammel[1], **Aritra Mukherjee**[2], **Luca Brandt**[2,3] **and Jannike Solsvik**[1]

[1]Department of Chemical Engineering, NTNU – Norwegian University of Science and Technology, 7491 Trondheim, Norway

[2]Department of Energy and Process Engineering, NTNU – Norwegian University of Science and Technology, 7491 Trondheim, Norway

[3]Department of Environment, Land and Infrastructure Engineering (DIATI), Politecnico di Torino, Torino, Italy

Corresponding author: Sanjid S. Chirammel, sanjidcs17@gmail.com

(Received 10 September 2025; revised 26 December 2025; accepted 16 February 2026)

The present study investigates the mass transfer of a dilute species from a dispersed bubbly phase to a carrier liquid phase using interface-resolved simulations and proposes a phenomenological model for its transient dynamics. To this end, we individually vary several input parameters, i.e. the species diffusivity (the Schmidt number, Sc), the void fraction (α) and the bubble size (which affects the Galilei number Ga and Bond number Bo) – while maintaining conditions representative of air bubbles in water. For the parametric range – $Sc = 1$, 5 and 10; $\alpha = 0.5\,\%$, $1.9\,\%$ and $3.6\,\%$; and three initial bubble diameters $d_0 = 0.63$ mm (i.e. $Ga = 1.75$ and $Bo = 0.0125$), 1.2 mm ($Ga = 4.6$ and $Bo = 0.045$) and 1.58 mm ($Ga = 7$ and $Bo = 0.07921$) – we show that increasing diffusivity and decreasing bubble size decreases scalar advection as compared with diffusion and hence the time needed for the species concentration to saturate in the carrier phase, which can be well represented by a Péclet number $Pe = \sqrt{gr_0}r_0/D_c$ based on the bubble rising speed, its radius and the species diffusivity. We also document the increase of the mass transfer rate with the void fraction when the carrier-phase scalar concentration is low, driven by a larger interfacial area and enhanced velocity fluctuations. When the species-rich bubble wakes start to interact, however, the transfer rate decreases, which occurs earlier at higher values of α. The proposed phenomenological model agrees closely with simulations, capturing a self-similar temporal evolution of the mean carrier-phase concentration. By rescaling the non-dimensional time τ as $Sc^{2/3}Ga/\alpha^{0.45}$, the numerical results collapse onto a master curve.

Key words: multiphase flow, gas/liquid flow, coupled diffusion and flow

© The Author(s), 2026. Published by Cambridge University Press. This is an Open Access article, distributed under the terms of the Creative Commons Attribution licence (https://creativecommons.org/licenses/by/4.0/), which permits unrestricted re-use, distribution and reproduction, provided the original article is properly cited.

https://doi.org/10.1017/jfm.2026.11338 Published online by Cambridge University Press

1. Introduction

Species transfer from buoyancy-driven bubbles is a widely utilised process in diverse applications, including chemical engineering (Shu *et al.* 2019; Kure, Jakobsen & Solsvik 2023; Mezui, Obligado & Cartellier 2023), bioprocessing (Doran 2013) and environmental sciences (Pashaei, Zarandi & Ghaemi 2017; Chai, Ngu & How 2022). These rising bubbles serve as an effective, passive and scalable means of enhancing mass transfer in these systems. Achieving reliable predictions, however, requires a detailed understanding of the coupled dynamics among hydrodynamics, mixing and interfacial transport. The present study addresses this need through direct numerical simulation (DNS), with a focus on how buoyancy-driven bubbly flows influence mass transfer rates. While experimental studies are valuable, they are often constrained by the challenges of accurately resolving small-scale interfacial mass transfer rates and systematically varying large-scale control parameters.

Interface-resolved DNS, as proposed here, have utilised various interface-capturing methods, such as the volume of fluid method, level set method, front tracking (FT) method, phase field method etc., and have provided new insights into buoyancy-driven bubble dynamics, advancing initial models based on potential flow theory (Sangani & Didwania 1993; Smereka 1993). Below is a brief summary of numerical studies investigating the hydrodynamics of buoyant bubbles.

The investigation of multiple rising bubbles began with the FT simulations of two bubbles in both two- (2-D) and three-dimensional (3-D) systems (Unverdi & Tryggvason 1992*a*,*b*). Subsequent work examined the liquid-side velocity field, revealing energy transfer from low-Reynolds-number (Re) bubbles to large-scale flow instabilities, demonstrated using 144 and 324 bubbles in 2-D domains (Esmaeeli & Tryggvason 1996). These findings were later validated by particle image velocimetry (Murai *et al.* 2000). The irregular motion of non-interacting 2-D bubbles was shown to increase with bubble size (Göz *et al.* 2000). While 2-D simulations capture rise velocity trends, 3-D computations are essential for accurate bubble distribution dynamics (Esmaeeli & Tryggvason 1999). Regarding collective bubble dynamics, the average rise velocity of eight bubbles in a 3-D periodic domain (defined as an evolving array) was computed and compared with the simulation of a single bubble in a periodic domain (defined as a regular array) (Esmaeeli & Tryggvason 1998, 1999). The bubbles in an evolving array rise faster than in a regular array at low Reynolds number ($Re \sim 1$–2, equivalent to Galilei number $Ga \sim 1.35 \times 10^{-2}$ and Bond number $Bo \sim 3.23 \times 10^{-4}$) and slower at moderate Reynolds number ($Re \sim 10{-}30$, $Ga \sim 10.33$ and $Bo \sim 0.48$).

On increasing the number of simulated 3-D bubbles to 27 in a fully periodic domain with void fraction up to 6 %, spherical bubbles were found to be non-interacting while ellipsoidal bubbles tended to form a stream (Bunner & Tryggvason 1999, 2003). At higher Re ($\approx \mathcal{O}(100)$), the deformable bubbles break the columnar structure and become randomly distributed with increased energy dissipation than for spherical bubbles (Esmaeeli & Tryggvason 2005). To compute the average drift velocity of 3-D bubbles, simulations incorporating up to 216 bubbles with void fractions ranging from 2 % to 24 % indicated that a minimum of 12 bubbles was sufficient in a fully periodic domain (Bunner & Tryggvason 2002*a*,*b*); this finding was subsequently extended to small and intermediate void fractions (Loisy, Naso & Spelt 2017). At higher void fractions, several interesting phenomena–drafting–kissing–tumbling and horizontal clustering–were reported (Bunner & Tryggvason 2002*a*,*b*; Zhang *et al.* 2021). Horizontal clustering, which increases drag, had previously been observed in simulations (Roghair, van Sint Annaland & Kuipers 2010) and was later confirmed experimentally at moderate Reynolds number ($Re \sim 90{-}250$, $Ga \sim 54$ and $Bo \sim 0.06$), where clusters formed and subsequently

https://doi.org/10.1017/jfm.2026.11338 Published online by Cambridge University Press

broke up (Figueroa-Espinoza & Zenit 2005). However, such clustering was absent at high Reynolds number ($Re = 800,\ Ga \sim 138,\ Bo \sim 0.21$) in experiments involving air bubbles of radius 1.25 mm injected into water at void fractions of 0.5 % and 1.05 % (Risso & Ellingsen 2002). In bi-dispersed systems, simulations by Göz *et al.* (2002) at a void fraction of 6 %, consisting of 29 larger and 29 smaller bubbles in a fully periodic domain, revealed that larger bubbles exhibit horizontal clustering similar to mono-dispersed systems, while smaller bubbles aligned vertically. Furthermore, correlations for the drag coefficient of both mono-dispersed (Roghair *et al.* 2011) and bi-dispersed (Roghair *et al.* 2013) bubble swarms have been proposed using DNS.

Similar studies on the hydrodynamics of multiple bubbles have also focused on vertical channel flows. In laminar down-flow, bubbles are displaced away from the walls, resulting in a homogeneous core region (Tryggvason, Lu & Biswas 2006), while in turbulent down-flow, a bubble-free wall layer is observed (Lu & Tryggvason 2006). In contrast, up-flow drives bubbles towards the walls, forming a wall layer in both Newtonian (Tryggvason *et al.* 2006) and viscoelastic (Ahmed *et al.* 2020) fluids. This behaviour is further modulated by bubble deformability and the presence of surfactants. In turbulent bubbly up-flow, void fraction distribution is more strongly influenced by bubble deformability than by bubble size (Lu & Tryggvason 2008), and high surfactant concentrations cause bubble clustering near the channel core rather than along walls (Lu, Muradoglu & Tryggvason 2017). Variation in bubble deformability can induce abrupt transitions between wall clustering, which leads to lower flow rates, and bulk clustering, which enhances flow rates (Dabiri, Lu & Tryggvason 2013). Results of DNS of bubbly flow in a vertical channel (Tryggvason, Ma & Lu 2016; Feng *et al.* 2019; Ma *et al.* 2020) and a periodic rectangular channel (Ma *et al.* 2017) have been also utilised for improved turbulence modelling. Beyond these commonly studied configurations – fully periodic and vertical channels – the dynamics of bubbles in 2-D rectangular channels with top and bottom no-slip boundaries remains scarcely explored. Coalescence of multiple bubbles has been investigated by varying the Morton number (Smolianski, Haario & Luukka 2008) or by applying a periodically oscillating pressure gradient (Lin *et al.* 2018). Bubble distributions in channel flows have also been examined under varying shear rates and imposed pressure oscillations in zero-gravity conditions (Lin *et al.* 2019). While the FT method remains widely utilised for simulating bubbly flows, recent studies have increasingly adopted coupled level set/volume-of-fluid (Nemati *et al.* 2021) and conservative level set (Balcázar-Arciniega *et al.* 2019) methods.

Besides the hydrodynamics of multiple bubbles, their influence on scalar transfer, such as heat and mass transfer, is of considerable industrial relevance. The effects of heat transfer have been extensively investigated in laminar bubbly flows (Annaland, Deen & Kuipers 2005; Deen & Kuipers 2013; Bhuvankar & Dabiri 2018; Panda *et al.* 2019; Zarei *et al.* 2025) and turbulent channel flows (Tanaka 2011; Piedra *et al.* 2015; Gvozdić *et al.* 2018). In addition to heat transfer, mass transfer also plays a critical role in numerous natural and industrial processes, where rising bubbles enhance the transport of species between phases. This transfer process depends on the complex interplay among bubble-induced flow, interfacial dynamics and the surrounding fluid properties. In bubbly flows, mass transfer is governed not only by the characteristics of the individual bubbles but also by the collective effects arising from interactions between the bubbles. A thorough understating and quantification of these mechanisms are essential for accurate modelling and optimisation in chemical engineering, bioprocessing and environmental applications. Nevertheless, detailed computational investigations of these complex mass transfer processes are still limited.

https://doi.org/10.1017/jfm.2026.11338 Published online by Cambridge University Press

Regarding mass transfer from multiple bubbles in a periodic domain, the flux from a fixed array (single bubble in a periodic box) is found to be comparable to that from a freely evolving array (Aboulhasanzadeh & Tryggvason 2014). The time-averaged mass transfer is computed for longer time by assuming the species concentration in the carrier phase as zero outside the corresponding boundary layer. Interestingly, the reduction in mass transfer caused by the lower Reynolds number of freely rising bubbles was offset by enhanced transfer due to bubble interactions. To model this process, Aboulhasanzadeh *et al.* (2012) utilised a multiscale approach based on the boundary-layer approximation and validated using experiments for high Schmidt number ($Sc = 8260$) and Reynolds number ($Re = 350,\ Ga \sim 465,\ Bo \sim 9.34$) (Aboulhasanzadeh *et al.* 2013). Their method avoided the need for finer grids at high Sc by solving a parabolised species equation with a second-order boundary-layer profile, coupled to a finite-volume scheme away from the interface.

By varying the void fractions between 4 % and 40 %, only a minor increase in the liquid-side mass transfer coefficient was observed in simulations (Roghair, van Sint Annaland & Kuipers 2016). In contrast, experiments on oxygen dissolution from rising air bubbles in water reported a reduction in mass transfer with increasing void fraction, a discrepancy attributed to the difference in Schmidt numbers: low Sc $(= 1)$ in the simulations versus high Sc $(= 502)$ in the experiments, which delays saturation in the liquid phase (Colombet *et al.* 2011, 2015). Similar minor increase in mass transfer is also reported for low Sc $(= 1)$ and low void fraction $(0.167-0.229)$ in bubbly flows (Balcázar-Arciniega *et al.* 2019, 2024). A correlation for the Sherwood number in bubble-induced turbulent flows was proposed by Jin & Schlüter (2019), based on solving the species equation in both carrier and dispersed phases while assuming Henry's coefficient (defined as the ratio of the species concentration in the dispersed phase and carrier phase when the interface is at chemical equilibrium) as unity, thus neglecting interfacial discontinuities in concentration. Extending the previous work on the hydrodynamics of homogeneous bubbly flows and mass transfer (Loisy *et al.* 2017), the convective diffusivity in longitudinal and transverse directions is analysed showing higher convective contribution along the longitudinal direction (Loisy, Naso & Spelt 2018). More recently, the influence of bubble-induced turbulence on species transfer has been investigated using a single bubble (Farsoiya *et al.* 2023) and up to two bubbles in a periodic domain (Jin *et al.* 2023). Notably, Farsoiya *et al.* (2023) demonstrated that the mass transfer coefficient scales as $Sc^{-0.5}$ for a suspended bubble, while Jin *et al.* (2023) showed that vertical velocity fluctuations intensify with increasing void fraction.

The above survey highlights that while numerous studies have employed interface-resolved simulations to examine the hydrodynamics of multiple bubbles in fully periodic domains and channel flows, far fewer have focused on scalar transfer. Of particular interest here, species transfer in bubbly flows can be strongly influenced by bubble rise velocity, deformability and bubble–bubble interactions. Moreover, most previous studies considered the time-averaged behaviour of the species transfer by neglecting the species saturation in the carrier phase as shown in table 1; this is, however, essential to understand the time evolution of the mass transfer in several relevant configurations. The recent study of Mangani *et al.* (2024) on heat transfer from heated dispersed drops/bubbles in turbulent channel flow further underscores the importance of such time-dependent analysis.

To conclude, this study has two objectives: (i) to investigate the time-dependent dynamics of species transfer from a buoyancy-driven dispersed phase allowing saturation in the carrier phase while varying governing parameters such as bubble size, which determines both the Galilei number (Ga) and Bond number (Bo), the void fraction (α) and the rate of species diffusion, i.e. the Schmidt number (Sc); and (ii) to propose a phenomenological model for the mass flux when varying these different governing non-

https://doi.org/10.1017/jfm.2026.11338 Published online by Cambridge University Press

Authors	Density ratio	Maximum Sc	Henry's coefficient (H_e)	Temporal analysis
Aboulhasanzadeh & Tryggvason (2014)	10	100	—	Time-averaged
Roghair *et al.* (2016)	800	1	0.8371	Time-averaged
Jin & Schlüter (2019)	828	4	1	Time-averaged
Balcázar-Arciniega *et al.* (2024)	100	1	—	Time-averaged
Present	833	10	33	Transient

Table 1. Previously published and present work on species transfer in buoyancy-driven bubbly flows within fully periodic domain.

dimensional numbers. For the first objective, the conservative diffuse interface (CDI) method (as previously suggested in Mirjalili, Jain & Mani (2022)) is implemented and validated by solving the species transport in both carrier and dispersed phase with Henry's coefficient (H_e) for discontinuous species concentration across the interface. For the second objective, a phenomenological model inspired by the results for heat transfer at different Prandtl numbers (Pr) by Mangani *et al.* (2024) is extended here for species transfer under varying Sc, α and bubble size in regimes characterised by limited bubble deformation and interactions.

This paper is organised as follows. In § 2, the governing equations utilised in this study and their solution procedure are presented. In § 3, we verify the numerical methodology and introduce the problem set-up. A detailed discussion of the results obtained is presented along with a proposed phenomenological model in § 4. Finally, we summarise the main findings and present some final considerations in § 5.

2. Computational details

This section on the computational methodology introduces the mathematical formulation used to study mass transfer in dilute conditions and the numerical discretisation and algorithm used to obtain a numerical solution of the problem at hand in § 2.1. Further, the capability of the current CDI-based in-house solver for species transfer from rising bubbles is demonstrated in § 2.2.

2.1. *Mathematical formulation and numerical methodology*

The problem consists of a two-fluid system with species transfer, mathematically modelled using conservation of mass and momentum, along with an interface advection equation. The unsteady flow field in the dispersed and carrier phases is modelled using the Navier–Stokes equations, whereas the species transfer from a dispersed gas phase to the liquid carrier phase is modelled using a scalar transport equation with interfacial mass transfer (Slattery 1999; Ishii & Hibiki 2010). We adopt a one-fluid formulation for the conservation of mass and momentum, resulting in one velocity (also used for the advection of interface) and pressure field, whereas a two-scalar model is adopted for species transfer (conservation of species). This is given as follows.

Phase field advection (interface advection equation):

$$\frac{\partial \phi}{\partial t} + \boldsymbol{\nabla} \cdot (\boldsymbol{u}\phi) = \boldsymbol{\nabla} \cdot \boldsymbol{r}, \tag{2.1}$$

where ϕ, t and $\boldsymbol{u}$ denote the phase-field function (assuming the values 0 and 1 in the pure phases), time and the velocity vector. The vector field $\boldsymbol{r}$ defines an interface regularisation

https://doi.org/10.1017/jfm.2026.11338 Published online by Cambridge University Press

term, defined as

$$\boldsymbol{r} = \gamma \left(\epsilon \nabla \phi - \phi(1-\phi) \frac{\nabla \phi}{|\nabla \phi|} \right), \tag{2.2}$$

where ϵ and γ are parameters defining the interface thickness and interfacial velocity of relaxation to the equilibrium shape. This term counteracts numerical diffusion and enforces a constant interface thickness during the numerical integration of the governing equations (Mirjalili *et al.* 2020, 2022).

Conservation of mass (continuity equation):

$$\nabla \cdot (\rho \boldsymbol{u}) = 0. \tag{2.3}$$

Here, ρ is the mixture density, defined as a weighted average:

$$\rho = \phi \rho_d + (1-\phi)\rho_c. \tag{2.4}$$

Conservation of momentum (Navier–Stokes equation):

$$\frac{\partial \rho \boldsymbol{u}}{\partial t} + \nabla \cdot ((\rho \boldsymbol{u} - (\rho_c - \rho_d)\boldsymbol{r})\boldsymbol{u}) = -\nabla p + \nabla \cdot \left(\mu \left[\nabla \boldsymbol{u} + \nabla \boldsymbol{u}^T \right] \right) + (\rho - \bar{\rho})\boldsymbol{g} + \sigma \kappa \, |\nabla \phi| \,, \tag{2.5}$$

where p, μ, g, σ and κ and are pressure, coefficient of dynamic viscosity, acceleration due to gravity, surface tension coefficient and local interface curvature, respectively. The last term on the right-hand side represents the surface tension forces, localised at the interface by the gradient of the phase-field function. Like density, the viscosity μ is the phase average of the gas and liquid viscosity:

$$\mu = \phi \mu_d + (1-\phi)\mu_c. \tag{2.6}$$

Conservation of species (scalar transport equation):

Following the two-scalar model for species transfer with interfacial mass transfer in Mirjalili *et al.* (2022), the transport equation for the species concentration in the dispersed phase reads

$$\frac{\partial c_d}{\partial t} + \nabla \cdot (\boldsymbol{u} c_d) = \nabla \cdot \left[D_d \phi \nabla \left(\frac{c_d}{\phi} \right) \right] + J_d + \nabla \cdot \left(\boldsymbol{r} \frac{c_d}{\phi} \right) \tag{2.7}$$

and similarly for the carrier phase

$$\frac{\partial c_c}{\partial t} + \nabla \cdot (\boldsymbol{u} c_c) = \nabla \cdot \left[D_c (1-\phi) \nabla \left(\frac{c_c}{(1-\phi)} \right) \right] - J_c + \nabla \cdot \left(\boldsymbol{r} \frac{c_c}{(1-\phi)} \right), \tag{2.8}$$

where c_i is the species concentration, D_i the coefficient of diffusivity and J_i the interfacial mass transfer term, with subscripts 'd' and 'c' for dispersed and carrier phases. The last terms guarantee a consistent transport of the scalar field in the interfacial region. See Mirjalili *et al.* (2022) for a detailed discussion on the derivation of the interfacial transfer term accounting for the scalar jump condition at the interface.

The above conservation equations are discretised on a staggered grid to avoid pressure–velocity decoupling (Rhie & Chow 1983) and pressure–interfacial force imbalance (Chirammel, Sharma & Murallidharan 2023). The CDI method adopted here has been recently used to consider evaporation (Salimi *et al.* 2025) and it is extended here to study mass transfer in dilute conditions. A full description of the code is reported in Salimi *et al.* (2025) and references therein.

This mass-conserving CDI method utilises the stability and boundedness criterion for the phase-field function in Mirjalili, Ivey & Mani (2020) to maintain a positive

https://doi.org/10.1017/jfm.2026.11338 Published online by Cambridge University Press

and bounded value of ϕ $(0 \leqslant \phi \leqslant 1)$; throughout this study we selected $\epsilon = \Delta x$ and $\gamma = |\boldsymbol{u}_{max}|$, where $|\boldsymbol{u}_{max}|$ is the maximum magnitude of the velocity vector within the computational domain. For the scalar c to be positive in the dispersed and carrier phases, besides the consistent discretisation of the advection term in the momentum equation, the mesh-resolution-based criterion given in Jain & Mani (2020) is followed. As regards time integration, the time step of the simulations is based on the shortest characteristic time scale among the different physical processes at play, as detailed in Salimi *et al.* (2025).

For multiple bubbles, the problem is defined by the different non-dimensional numbers defined below:

$$\begin{aligned} &\text{Galilei number, } Ga = \frac{\rho_c \sqrt{g} r_0^{3/2}}{\mu_c}; \quad && \text{Bond number, } Bo = \frac{\rho_c g r_0^2}{\sigma}; \\ &\text{Schmidt number, } Sc = \frac{\nu_c}{D_c}; && \text{void fraction, } \alpha = \frac{N_b \times v_b}{l_x \times l_y \times l_z}, \end{aligned} \tag{2.9}$$

where v_b is the initial volume of a single bubble and N_b is the total number of bubbles in a computational domain of size $l_x \times l_y \times l_z$. The Galilei number indicates the ratio of buoyancy force to viscous forces and affects directly the bubble rising speed and the wake past the bubbles. The Bond number is a non-dimensional measure of the importance of buoyancy with respect to surface tension, and is therefore a measure of the bubble deformability (with deformability increasing with Bo). Finally, the Schmidt number is the ratio between momentum and species diffusion.

2.2. *Validation, grid independence and mass conservation studies*

The current CDI implementation has been validated against several benchmark multiphase flows including isothermal and non-isothermal evaporation with volume shrinkage (Salimi *et al.* 2025). In this study of interfacial mass transfer from dispersed to carrier phase without volume shrinkage, we consider scalar transfer from a suspended bubble, scalar transfer from a rising bubble and the scaling of the scalar boundary-layer thickness for further comparisons with analytical and published numerical results. As regards the scalar transfer from a suspended bubble, we use the computational set-up shown in figure 1(*a*). All the transport and physical properties are specified in dimensional form and assigned a value of unity, except for the diffusion coefficient which is set to $5 \times 10^{-5}\ \mathrm{m^{-2}\ s}$, and compare the transient scalar distribution with the analytical solution in Crank (1975). Good agreement between the simulation and the analytical solution is obtained as shown in figure 1(*b*). For the scalar transfer from a 2-D rising bubble, the previously published volume-of-fluid-based numerical result of Bothe & Fleckenstein (2013) is utilised for comparing the time evolution of the spatially averaged or mean oxygen concentration ($\overline{c}_b$). Considering the density ratio χ $(= \rho_d/\rho_c) = 1.2 \times 10^{-3}$, viscosity ratio η $(= \mu_d/\mu_c) = 1.8 \times 10^{-3}$, acceleration due to gravity $g = 9.8\ \mathrm{m\,s^{-2}}$, surface tension coefficient $\sigma = 0.078\ \mathrm{N\,m^{-1}}$, diffusion coefficient of oxygen in water (carrier phase) $D_c = 10^{-6}\ \mathrm{m^{-2}\ s}$ and Henry's coefficient $H_e = 33$, the output parameters are non-dimensionalised using the initial radius of the bubble ($r_0 = 0.0005$ m) as length scale l_c, rise velocity u_b as velocity scale u_c and l_c/u_c as time scale t_c. Utilising the computational set-up shown in figure 1(*c*), the quantitative validation against the results of Bothe & Fleckenstein (2013) is reported in figure 1(*d*). We performed simulations with three different grid resolutions, $r_0/8$, $r_0/16$ and $r_0/32$, in a 2-D computational domain of size $16r_0 \times 32r_0$, and report a maximum relative error of 0.57 % and 0.17 % for the two finest grids under consideration ($r_0/16$ and $r_0/32$) with a percentage deviation of 0.74 % between the finest grids. The same rising bubble is simulated for different Schmidt numbers on a 3-D Cartesian mesh

https://doi.org/10.1017/jfm.2026.11338 Published online by Cambridge University Press

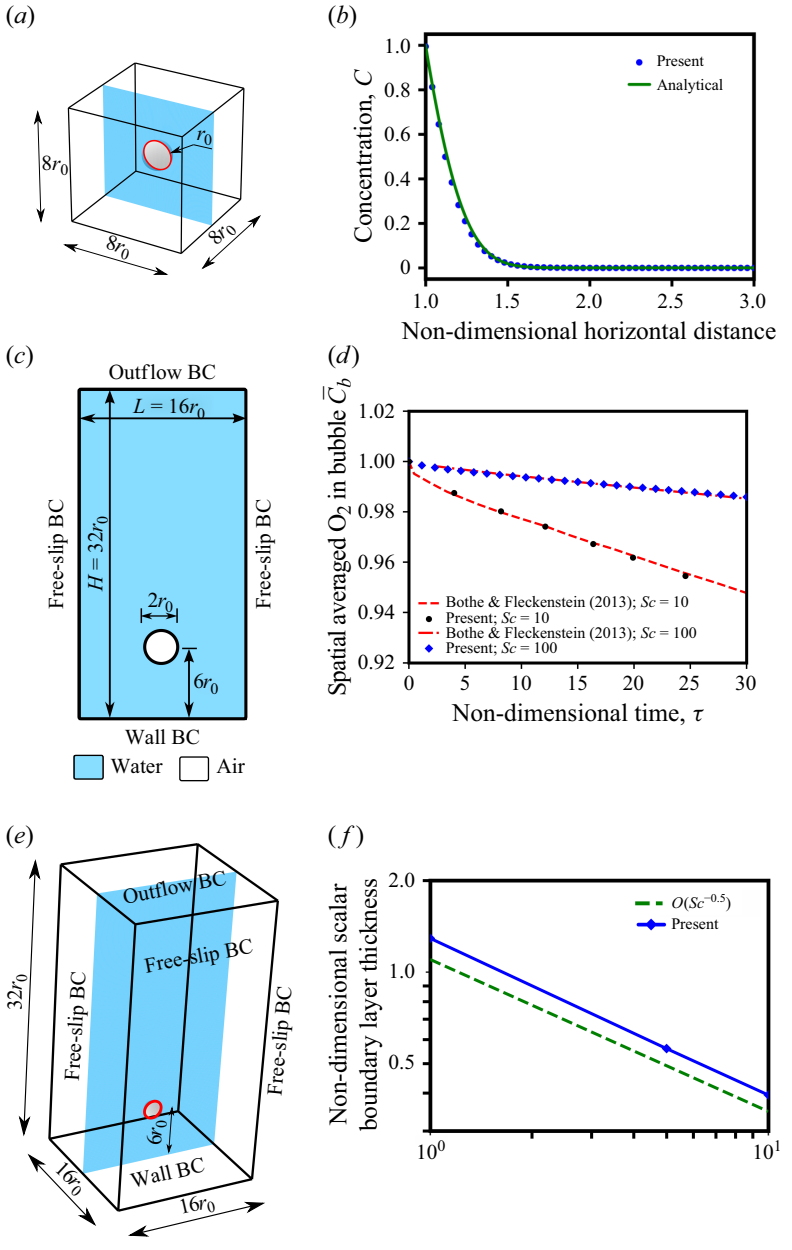


Figure 1. Validation of the current numerical implementation on 2-D and 3-D Cartesian mesh. The computational set-up corresponds to scalar transfer from (*a*) a suspended bubble, (*c*) a 2-D rising bubble and (*e*) a 3-D rising bubble. For each of these three cases the respective validations are shown in (*b*,*d*,*f*).

(see figure 1*e*) and for the same transport and physical properties to estimate the scalar boundary-layer thickness at the bubble equatorial position once a steady state is reached. Figure 1(*f*) shows that the time evolution of the scalar boundary layer follows a -0.5 scaling, which is in good agreement with the theory of Bothe & Fleckenstein (2013) and Weiner & Bothe (2017). Finally, figure 2 shows the capability of our numerical tool to simulate a rising bubble without any mass leakage, essential for the simulation of multiple rising bubbles over a longer time, as investigated in this study.

https://doi.org/10.1017/jfm.2026.11338 Published online by Cambridge University Press

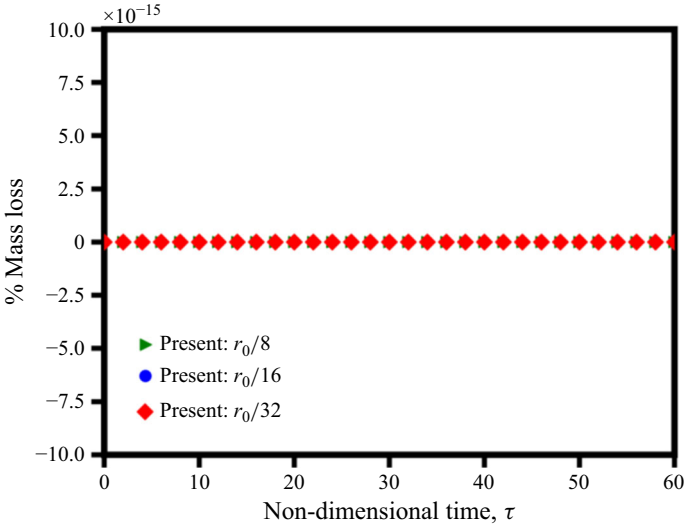


Figure 2. Time evolution of the mass loss with the present CDI method for a 3-D rising bubble; see set-up in figure 1(*e*).

3. Problem set-up and parametric details

We investigate mass transfer from multiple rising bubbles in a periodic domain, mimicking the process in a bubble column of size significantly larger than our computational domain and far from solid boundaries.

The choice of the number of bubbles, $N_b = 12$, is motivated by the previous simulations of multiple bubbles in periodic domains by Bunner & Tryggvason (2002*a*). Those authors have shown that the average bubble rising velocity becomes almost independent of the number of bubbles when $N_b \geqslant 12$. Note that they also reported that the bubble velocity fluctuations and the Reynolds stresses in the liquid phase increase with the number of bubbles and no limiting behaviour was observed even with 216 bubbles (Bunner & Tryggvason 2002*b*). Therefore, the findings of the present work are restricted to the current configuration. As this study focuses on the effect of hydrodynamic interactions on species transfer rather than coalescence or breakage due to bubble–bubble interactions, the simulations are initiated with a random bubble distribution with the minimum centre-to-centre distance between the bubbles of $4r_0$ as shown in figure 3; bubbles are placed sufficiently far from each other to prevent bubble–bubble direct interactions. From a series of preliminary simulations, it was observed that increasing the non-dimensional parameters Ga, Bo and α favours bubble coalescence. Hence, the largest Ga, Bo and α are selected such that bubble coalescence is avoided throughout the simulation. As concerns the Schmidt number, the high resolution needed at low diffusivity and corresponding computational costs prevented using values of $Sc > 10$ to be able to perform the rich parameter study presented here. Also, as the time scale associated with liquid saturation with O_2 compared with the time scale for its complete removal from air bubbles is significantly shorter, the assumption of constant bubble volume can be safely adopted in this study.

The input values for all cases under consideration in this study are reported in table 2. The transport and physical properties of the fluids correspond to oxygen transfer from air bubbles to water, like the validation case in § 2.2, with a reduced Schmidt number to make the computations affordable. The input non-dimensional parameters such as bubble size, i.e. (Ga, Bo), Sc and α are varied by changing r_0, D_c and the size of the

https://doi.org/10.1017/jfm.2026.11338 Published online by Cambridge University Press

Input parameter	Values
r_0	0.315 mm ($Ga = 1.75$ and $Bo = 0.0125$) 0.6 mm ($Ga = 4.6$ and $Bo = 0.045$) 0.79 mm ($Ga = 7$ and $Bo = 0.07921$)
Sc	1, 5, 10
Sc_r	0.33, 1.67, 3.33
α	0.5 %, 1.9 %, 3.6 %

Table 2. List of the input parameters for the different simulations presented here, with Sc_r representing the ratio of Sc in carrier phase to dispersed phase. At time zero, the concentration in the dispersed phase $\overline{C}_d(\boldsymbol{x}, t = 0) = 1$, whereas in the carrier phase $\overline{C}_c(\boldsymbol{x}, t = 0) = 0$. All the non-dimensional numbers are calculated with $g = 9.8\ \mathrm{m\,s^{-2}}$ and $\sigma = 0.078\ \mathrm{N\,m^{-1}}$.

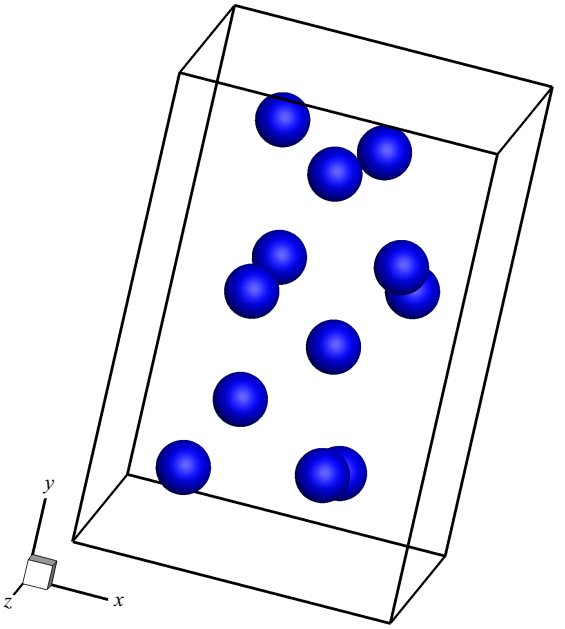


Figure 3. A schematic showing the initial arrangement of 12 bubbles in the periodic computational domain (non-dimensional time, $\tau = 0$) for the present simulations. The bubble interface separating air and water is shown by the blue contour corresponding to the value of the phase-field function ($\phi = 0.5$).

computational domain ($l_x \times l_y \times l_z$). Note that when varying the bubble diameter, Ga and Bo vary simultaneously, which results in values of Ga within the range $1.75-7$ and Bo within $0.01250-0.07921$ for initial bubble radii in the range $0.315-0.790$ mm. All the simulations are initiated with quiescent fluid and a uniform initial concentration in the dispersed phase without any dissolved species in the carrier phase. Periodic boundary conditions are imposed for velocity and scalar fields and the simulations are performed on a finer grid of $r_0/32$, sufficient to capture the hydrodynamics and species distribution. To obtain the results presented below, each case was simulated with a message-passing interface-based decomposition of the computational domain and run on 512 cores on the Betzy supercomputer at NRIS, Norway.

The role of the different input parameters in the species mass transfer from the rising bubbles is investigated by considering the time evolution of the normalised mean

https://doi.org/10.1017/jfm.2026.11338 Published online by Cambridge University Press

concentration in the dispersed and carrier phases, denoted as $\overline{C}_d$ and $\overline{C}_c$, respectively, and computed as

$$\overline{C}_d = \frac{\mathscr{C}_d}{\mathscr{C}_{d,0}} \quad \text{and} \quad \overline{C}_c = \frac{\mathscr{C}_c}{\mathscr{C}_{d,0}}, \tag{3.1}$$

where

$$\begin{aligned} \mathscr{C}_d &= \frac{\int_0^{l_z}\int_0^{l_y}\int_0^{l_x}(c_{d,(x,y,z)}\phi)\,\mathrm{d}x\,\mathrm{d}y\,\mathrm{d}z}{\int_0^{l_z}\int_0^{l_y}\int_0^{l_x}\phi\,\mathrm{d}x\,\mathrm{d}y\,\mathrm{d}z}, \\ \mathscr{C}_c &= \frac{\int_0^{l_z}\int_0^{l_y}\int_0^{l_x}c_{c,(x,y,z)}(1-\phi)\,\mathrm{d}x\,\mathrm{d}y\,\mathrm{d}z}{\int_0^{l_z}\int_0^{l_y}\int_0^{l_x}(1-\phi)\,\mathrm{d}x\,\mathrm{d}y\,\mathrm{d}z}, \end{aligned} \tag{3.2}$$

where $\mathscr{C}_d$ and $\mathscr{C}_c$ are the volume-averaged species concentration in the dispersed and carrier phases, respectively. These are further normalised with the initial values in the dispersed phase $\mathscr{C}_{d,0}$. Finally, the presented results are normalised for length ($\boldsymbol{x}$), velocity ($\boldsymbol{u}$) and time (t) with the initial bubble radius (r_0), the characteristic velocity scale ($u_c = \sqrt{gr_0}$) and convective time scale ($t_c = r_0/u_c$) as given below:

$$\boldsymbol{X} = \frac{\boldsymbol{x}}{r_0}; \quad \boldsymbol{U} = \frac{\boldsymbol{u}}{u_c}; \quad \tau = \frac{tu_c}{r_0}, \tag{3.3}$$

where $\boldsymbol{X}$, $\boldsymbol{U}$ and τ are non-dimensional length, velocity and time.

4. Results and discussion

This section presents and discusses the results of the interface-resolved simulations of multiple rising bubbles in three different subsections. The first subsection focuses on the qualitative description of the species transfer, while the second and third subsections examine the quantitative and self-similar characteristics of species transfer, considering the variations in the input parameters introduced above and propose a parametrisation of the process through a phenomenological model.

4.1. *Flow statistics and qualitative analysis*

This section qualitatively discuss the behaviour of multiple bubbles for non-dimensional governing parameters $Ga = 7$, $Bo = 0.07$, $Sc = 10$ and $\alpha = 1.9\,\%$, and then extends the analysis to the different void fractions and bubble sizes considered in table 2. The bubbles, with initially random positions as shown in figure 3, rise due to buoyancy and undergo lateral motions due to wake interactions, maintaining a chaotic distribution throughout the simulation. This behaviour is shown at various time instances in figure 4(*a–c*) for a constant void fraction ($\alpha = 1.9\,\%$). Breakup of the initial arrangement (relative motion between the bubbles) is reported for 8 spherical bubbles at lower void fractions of $0.0335\,\%$, $0.0654\,\%$ and $0.1256\,\%$ in Esmaeeli & Tryggvason (1998) and for 27 spherical bubbles at $\alpha = 2\,\%$ in Bunner & Tryggvason (2003). A similar behaviour is obtained in the present study for the void fractions of $0.5\,\%$ and $3.6\,\%$ as shown in figures 4(*d*) and 4(*e*), respectively.

The instantaneous non-dimensional average rise velocity for the configurations with different α under investigation is shown in figure 5; in the figure, one can observe a short initial transient, with oscillations, before the final steady condition is attained. Note that, as discussed later, the time scales associated with the momentum fluxes are decoupled from those of the species transfer; in particular, the time needed to reach a steady average rising

https://doi.org/10.1017/jfm.2026.11338 Published online by Cambridge University Press

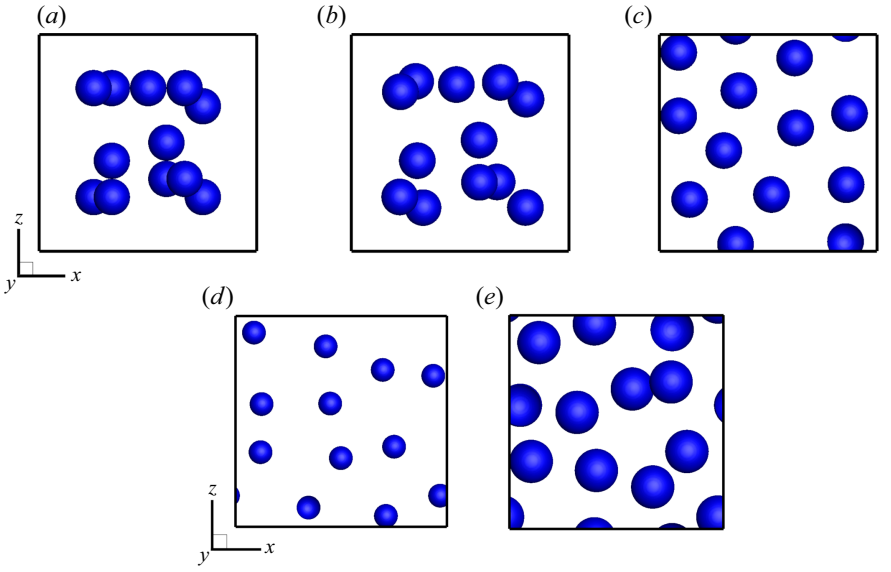


Figure 4. Top view of the lateral motion of rising bubbles with $Ga = 7$ and $Bo = 0.07921$ in the horizontal $x-z$ plane at various time instances and void fractions. For a constant void fraction of $\alpha = 1.9\,\%$, the distribution of bubbles in the computational domain is shown for non-dimensional times: (*a*) $\tau = 0$, the initial condition; (*b*) $\tau = 14$ (transient); and (*c*) steady condition at $\tau = 200$. The bubble distributions at $\tau = 200$ are displayed for different void fractions of (*d*) $\alpha = 0.5\,\%$ and (*e*) $\alpha = 3.6\,\%$ once a nearly steady average rising velocity is achieved. For clarity, the aspect ratio of the computational domain is kept similar, creating the illusion of varying bubble size. In the simulations, however, the bubble size is fixed and variations of α are obtained by varying the size of the computational domain.

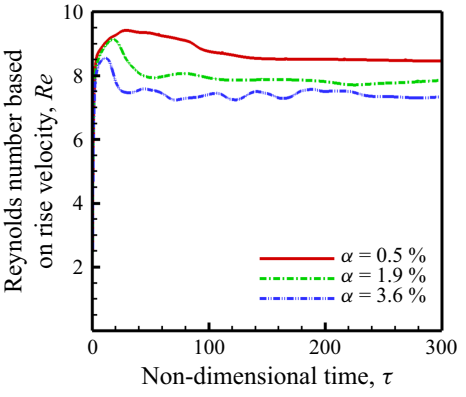


Figure 5. Time evolution of the Reynolds number based on the average rise velocity, $Re = (\rho_c r_0 v)/\mu_c$, where v is the volume-averaged dispersed-phase velocity in the vertical y direction, for the bubbles with initial diameter of 1.58 mm, corresponding to Galilei number $Ga = 7$ and Bond number $Bo = 0.07921$, for the various α indicated in the legend.

velocity is much shorter than that needed to have species saturation in the liquid phase and quench the mass transfer. Moreover, we observe that, as the void fraction increases, the bubble rising velocity decreases due to increased bubble clustering as evident in figure 4(*c–e*). A similar trend has also been shown by Bunner & Tryggvason (2002*a*) considering void fractions of 2 %, 6 %, 12 % and 24 %, with a machine oil as working fluid instead of air–water as in this study. The similarities with previously published data further

https://doi.org/10.1017/jfm.2026.11338 Published online by Cambridge University Press

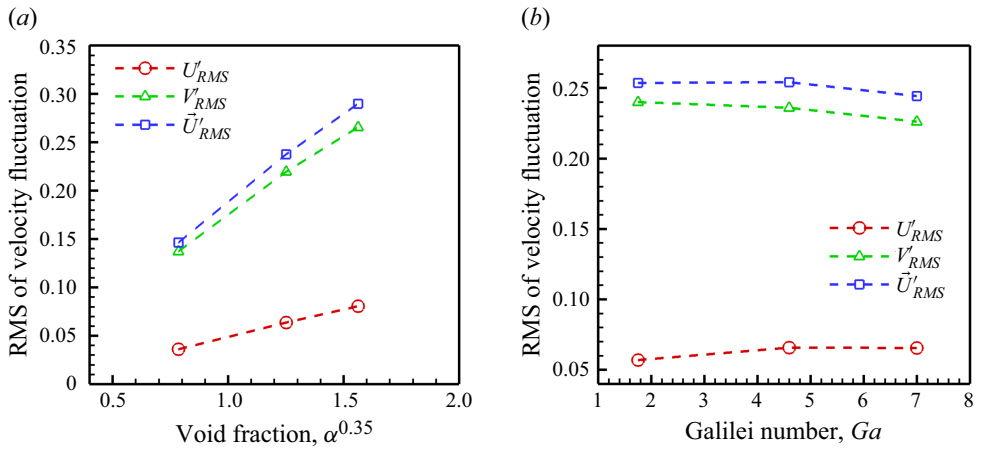


Figure 6. Variation of the RMS velocity fluctuations in the horizontal direction U'_{RMS} and vertical direction V'_{RMS}, and of the velocity vector $\boldsymbol{U}'_{RMS}$, for (*a*) different void fractions α and (*b*) different Galilei number Ga (bubble rising speed). The abscissa $\alpha^{0.35}$ is selected to display straight lines in linear scale.

demonstrate the capability of the present implementation to capture the hydrodynamics associated with multiple rising bubbles in a periodic domain.

To better interpret the data on mass transfer, we document the flow features in terms of root-mean-square (RMS) velocity fluctuation as shown in figure 6 for the different void fractions and Galilei numbers under investigation. The RMS of the componentwise velocity fluctuations is computed from the time-averaged volume integral of the local deviations of the velocity field from the mean velocity. The vector RMS is computed as the magnitude of the resulting velocity-fluctuation vector. The data in the figure reveal that the RMS of the velocity fluctuation scales with the void fraction as $\alpha^{0.35}$, while it remains nearly constant, in non-dimensional units, across the range of Ga considered; the latter implies that the velocity fluctuations are proportional to the bubble rise velocity. This exponent indicates that the velocity fluctuations scale to a good approximation with the average distance among bubbles, which is proportional to the void fraction raised to the power $1/3$. Higher values would be expected if bubbles deform more, as reported in the literature from experiments with larger bubble sizes, when the RMS is found to scale with the void fraction $\alpha^{0.4}$ (Riboux, Risso & Legendre 2010). As expected, the vertical velocity fluctuations are larger than the horizontal components, a signature of a laminar flow characterised by pronounced wakes; see also the visualisations in figure 7.

As mentioned earlier, the major focus of this study is on the time history of mass transfer from multiple rising bubbles. As the bubbles start rising through the initially stagnant carrier phase, the species confined within the dispersed phase start to dissolve into the carrier phase. The rate at which this dissolution occurs depends on various factors like Sc, α and bubble size, the former two affecting the rising speed and wake flow characteristics. As expected, the effect of increasing Sc is to reduce the species diffusion rate as evident in figures 7(*a*) and 7(*b*) for carrier-side Sc of 1 and 10, respectively. A significant variation in species concentration within the carrier phase can be observed on a vertical x–y plane at non-dimensional time $\tau = 20$; as a reference, the complete time evolution is shown in figure 8 and is discussed later. Note that the data in figure 7(*a*,*b*) are obtained by keeping the other governing parameters (Ga, Bo and α) constant, which implies the same bubble distribution and the same flow for these two cases. Even though the bubble dynamics remains the same – the flow field, and hence the velocity boundary layer around each

https://doi.org/10.1017/jfm.2026.11338 Published online by Cambridge University Press

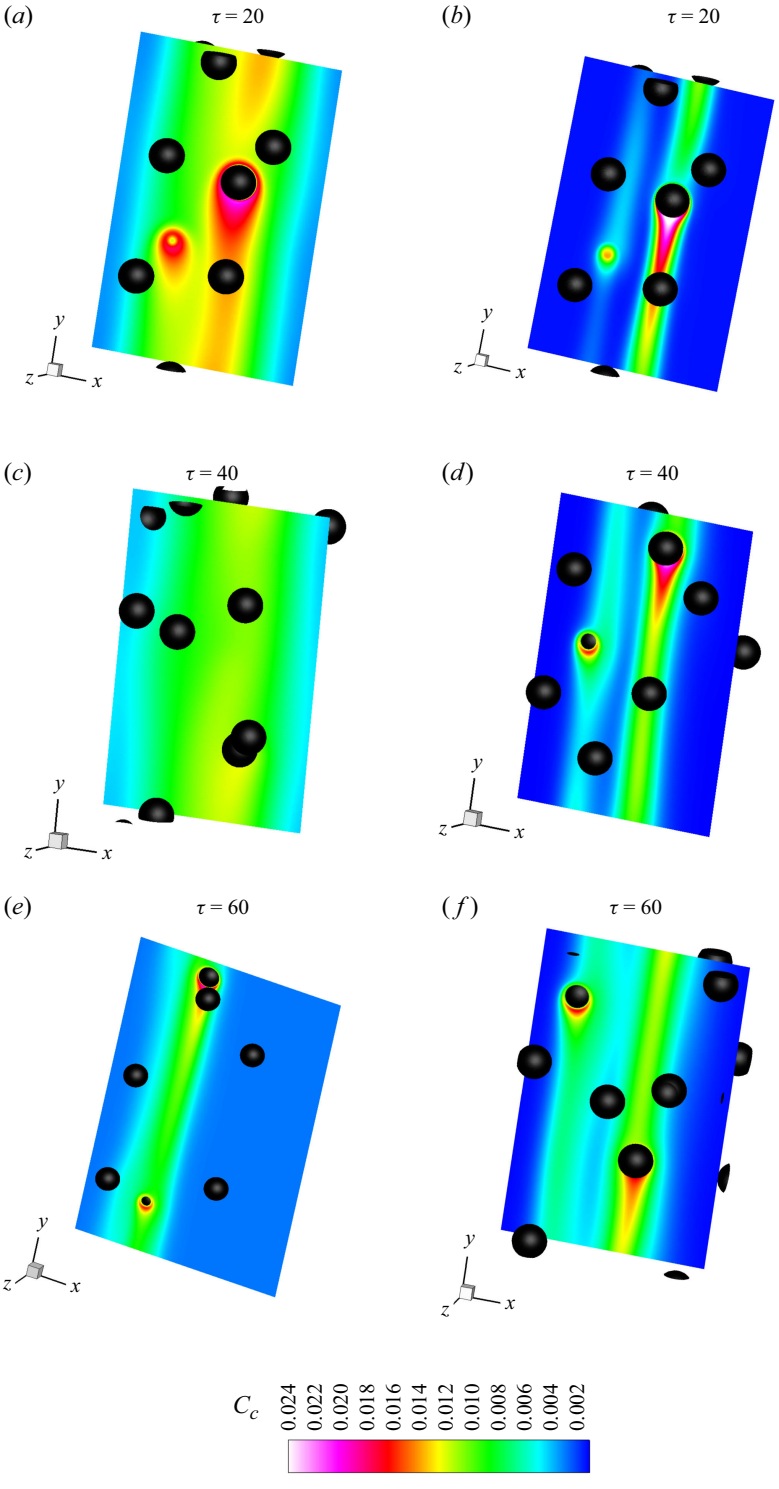


Figure 7. Species distribution in the carrier phase on a vertical $x-y$ plane for Schmidt numbers $Sc = 1$ and 10 (a,b), bubble sizes $r_0 = 0.315$ and 0.79 mm (c,d) and void fractions $\alpha = 0.5$ % and 3.6 % (e,f). Comparisons are made at the same non-dimensional time τ, though different values of τ are chosen for the different parameters to highlight the variation in species distribution.

https://doi.org/10.1017/jfm.2026.11338 Published online by Cambridge University Press

bubble, is not affected by the mass transfer in our model – the scalar boundary-layer thickness decreases for $Sc = 10$. Consequently, the scalar concentration is higher within the wake of the rising bubbles for $Sc = 10$, whereas it remains more uniformly distributed for $Sc = 1$. For the case of multiple bubbles or drops in turbulent channel flow, Mangani *et al.* (2024) have shown an increased temperature difference between carrier and dispersed phases when increasing Pr from 1 to 8.

To visualise the effect of the void fraction on the species distribution in the carrier phase, we display in figures 7(*c*) and 7(*d*) the scalar field in the x–y plane for $\alpha = 0.5\,\%$ and $\alpha = 3.6\,\%$, while keeping d_0 and Sc constant. In this case, the flow snapshot is taken at $\tau = 77$ (see the complete time evolution in figure 7). Increasing the relative volume of the dispersed phase, α, results in an early saturation in the carrier phase and therefore an almost uniform distribution of the species concentration; see discussion below for a quantitative analysis of the time evolution. Finally, we consider constant void fraction α and Schmidt number Sc, and examine the difference in the species distribution for different bubble diameters; see figures 7(*e*) and 7(*f*) for results with increasing D_0. Here, one can note more pronounced wakes and higher concentrations along vertical paths in the case of largest bubbles (note that for clarity bubbles have been visualised at a similar size).

4.2. *Effect of Schmidt number, void fraction and bubble size on mass transfer*

The different non-dimensional parameters influencing the flow characteristics are the Galilei number, the Bond number and void fraction (see figure 6 for their effect on the velocity fluctuations), whereas the Schmidt number only quantifies the rate of species diffusion. Note that, instead of varying Ga and Bo independently, we here vary the bubble size as one would do in an experiment with the same working fluids, which results in the simultaneous variation of Ga and Bo. Consequently, the effects of Ga and Bo are analysed in terms of bubble size, as discussed below. To investigate the effect of Sc, the diffusion coefficient is varied, while the initial bubble radius and void fraction remain constant. When examining the modulations of mass transfer with the void fraction α, we vary the size of the computational domain without changing the number of bubbles, their radius r_0 and the Schmidt number Sc. This yields domains of size $18 \times 27 \times 18$, $12 \times 18 \times 12$ and $10 \times 14 \times 10$ in units of initial bubble radius for $\alpha = 0.5\,\%$, $1.9\,\%$ and $3.6\,\%$, respectively. Note that, to maintain the needed computational accuracy, the grid size corresponds to $r_0/32$ in all cases, which implies that the total number of grid points is higher at lower void fraction $\alpha = 0.5\,\%$ than for the other two cases. In the following paragraphs, we quantitatively examine the effects of varying Sc, α and r_0 on the mass transfer. To measure this transfer between the two phases, we consider the time evolution of the spatially averaged (or mean) scalar concentration within the air bubbles (dispersed phase) and water (carrier phase).

The results pertaining to the different Sc are presented in figure 8, depicting the difference in rate of species transfer and associated time for the saturation of the phase-changing species concentration in the liquid phase. As shown in figure 8(*a*), the spatial average of the species concentration in the dispersed phase reduces with time and reaches a saturation value. Conversely, for the carrier phase (figure 8*b*), the dissolved species concentration increases, reaching a saturation value when the equilibrium at the interface is attained. A higher Sc reduces diffusion, delaying saturation in both the dispersed and carrier phases. The non-dimensional time to reach saturation increases from 69.65 to 370.86 as Sc increases from 1 to 10, while the final saturation concentration remains independent of Sc and is determined only by the void fraction. Also, the saturation species concentrations in the dispersed and carrier phases are different due to the discontinuity of the species concentration across the interface, as defined by Henry's coefficient (He).

https://doi.org/10.1017/jfm.2026.11338 Published online by Cambridge University Press

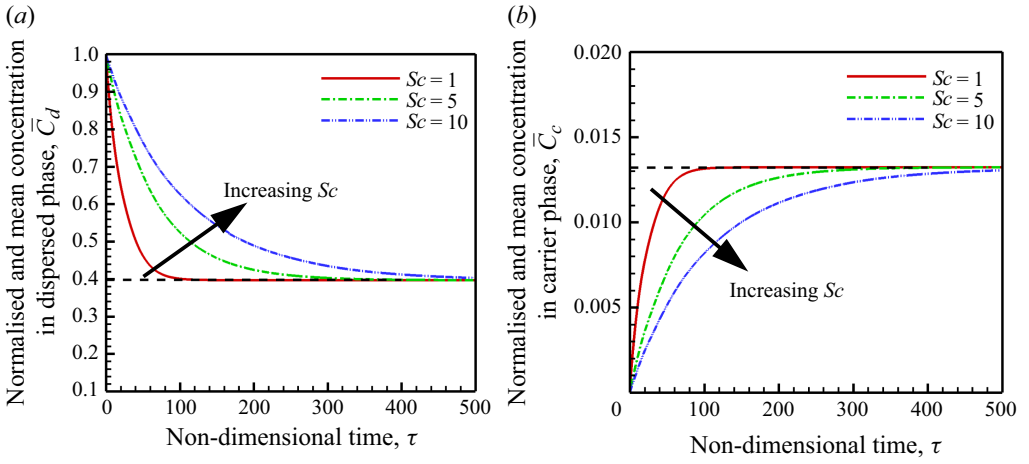


Figure 8. Time evolution of the normalised and averaged species concentration in (*a*) the dispersed phase and (*b*) the carrier phase for different carrier-side Schmidt number (Sc). The results are obtained at constant bubble size ($Ga = 7$ and $Bo = 0.07921$) and void fraction ($\alpha = 1.9\,\%$). The final equilibrium species concentrations in the carrier and dispersed phases are represented with black dashed lines.

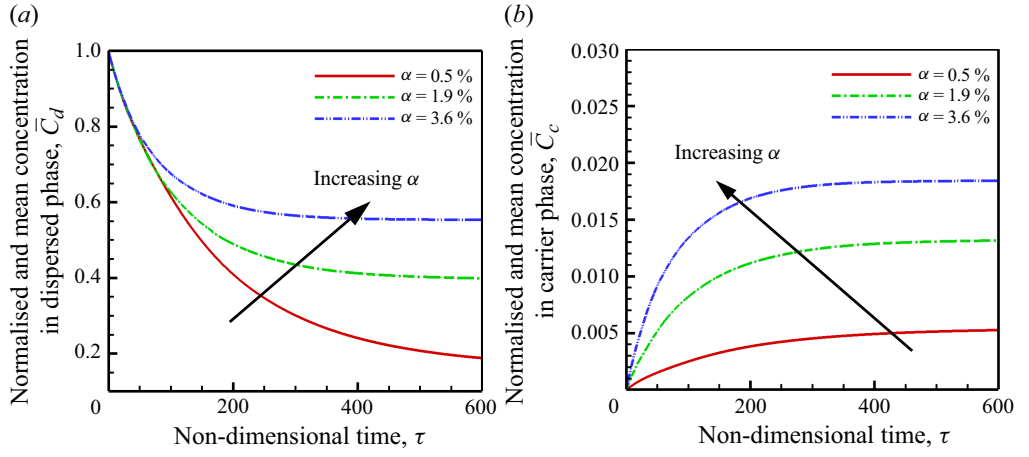


Figure 9. Time evolution of the normalised average species concentration in (*a*) the dispersed phase and (*b*) the carrier phase for different void fractions (α), as indicated in the legend. The void fraction α is varied while keeping the initial bubble size (corresponding to $Ga = 7$ and $Bo = 0.07921$) and Schmidt number ($Sc = 10$) constant.

The void fraction influences both the rate and the final level of saturation for the average scalar concentration in the dispersed and carrier phases as shown in figure 9. As expected, the final saturation values differ with void fraction α, whereas the variations of the Schmidt number only affect the time needed to reach equilibrium as discussed in the previous paragraph. Due to the geometrical constraint imposed by the chosen value of α, saturation is reached earlier at higher void fractions, when the liquid volume is minimum, which also explains the smallest value of the carrier-phase steady-state concentration for the largest void fraction at equilibrium. Moreover, we observe the transfer rates to increase with void fraction at earlier times, when the carrier phase is depleted of the scalar. Estimating the transfer rates from the data (see the initial slope in figure 9*b*), we observe an almost linear

https://doi.org/10.1017/jfm.2026.11338 Published online by Cambridge University Press

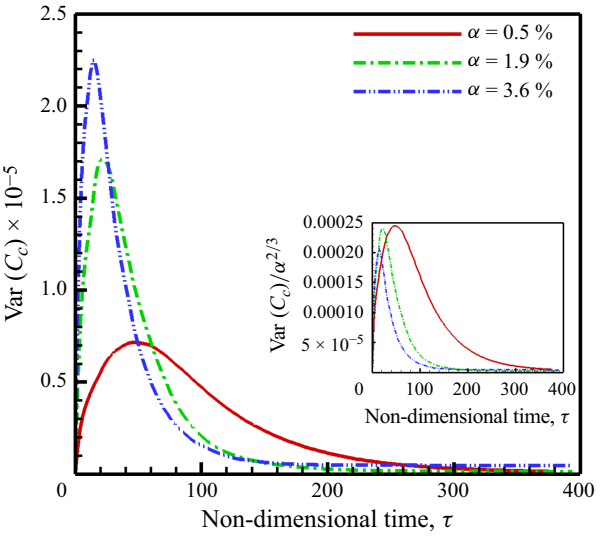


Figure 10. Time evolution of the variance of the scalar concentration within the carrier phase for the different void fractions under investigation, $\alpha = 0.5\,\%$, $1.9\,\%$ and $3.6\,\%$, and fixed values $Ga = 7$, $Bo = 0.07921$ and $Sc = 10$ (same cases as in figure 9). The inset illustrates the variance along the y axis, scaled by $\alpha^{2/3}$.

scaling of transfer rate with void fraction, $\sim\alpha^{0.9}$, which is faster than the only increase of the surface area ($\sim\alpha^{2/3}$). We therefore attribute the initially faster mass transfer to the combined effect of increased interfacial area and increased velocity fluctuations (see figure 6*a*). At later times, the species-rich wakes and boundary layers behind and around the bubbles start interacting, which slows down the average interfacial flux earlier for larger values of α.

The differences due to the different void fractions are further illustrated in figure 10, depicting the temporal evolution of the scalar concentration variance in the carrier phase, defined as

$$\mathrm{var}(C_c) = \left[\overline{C_c^2} - (\overline{C_c})^2\right]. \tag{4.1}$$

This observable variance shows a similar trend for all void fractions, with a sudden rise to a maximum value followed by a gradual reduction to the final steady value (zero indicating a uniform distribution in the carrier phase). As the scalar concentration is uniform and zero in the carrier phase at time $t = 0$, the variance starts from zero and increases to a peak value that is higher the larger the void fraction. As shown in the inset of figure 10, the initial peak is associated with the formation of the scalar boundary layers around the bubbles and is therefore proportional to the surface area, i.e. to the void fraction α. Soon the scalar diffuses further from the bubbles, and the variance reduces and approaches zero, indicating the homogeneous distribution in the carrier phase.

The effect of varying bubble sizes reported in figure 11(*a*,*b*) is similar to the effect of varying Sc (see figure 8). The final values of the scalar concentration are the same as we are considering constant void fraction, but the time needed to reach saturation increases with the bubble size, in other words it increases with the ratio between bubble velocity and diffusion. The same explanation can be given for the results in figure 8, where the increase in the ratio between bubble velocity and diffusion is instead obtained by reducing the species diffusion, also leading to an increase in the time to saturation. This is further confirmed in figure 12 which illustrates the average concentration versus time for all cases in figures 8 and 11 in terms of a Péclet number based on bubble size and velocity

https://doi.org/10.1017/jfm.2026.11338 Published online by Cambridge University Press

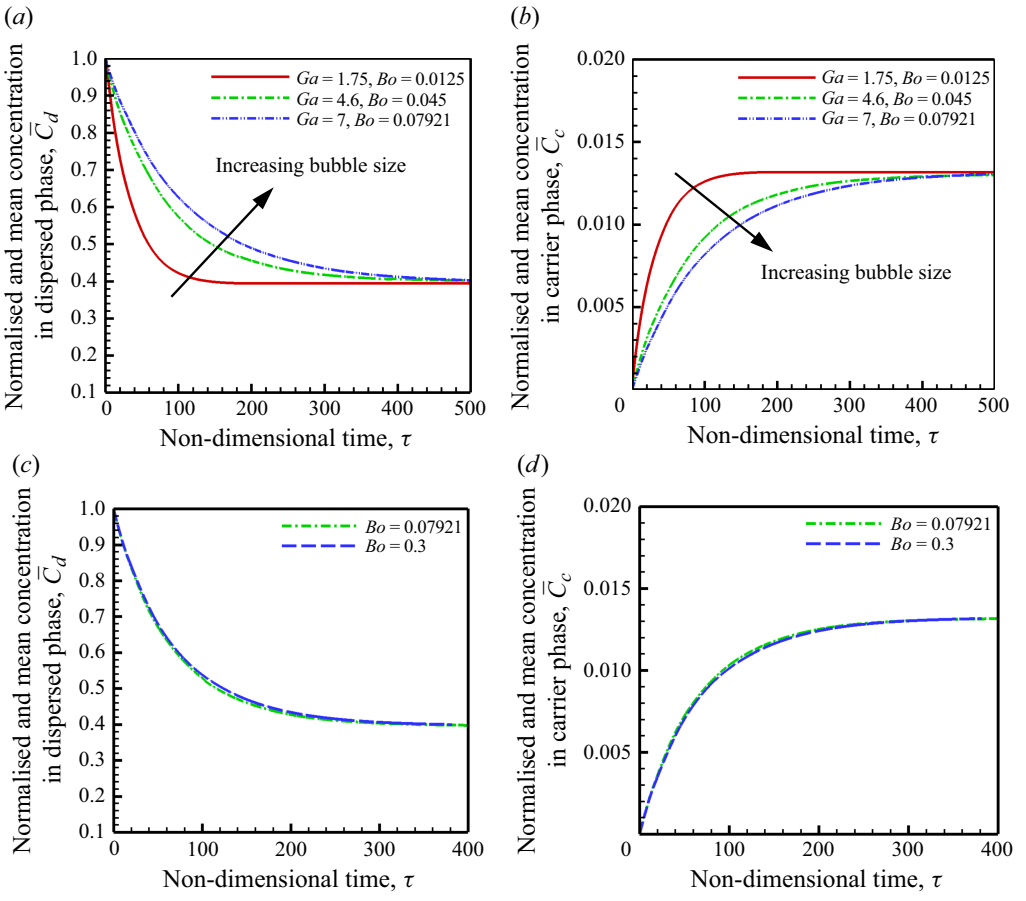


Figure 11. Time evolution of the normalised and averaged species concentration in (*a*) the dispersed phase and (*b*) the carrier phase for different bubble sizes, implying different values of the Galilei and Bond numbers (see legend). The bubble size is varied at fixed void fraction ($\alpha = 1.9\,\%$) and Schmidt number ($Sc = 10$). The average concentration in (*c*) the dispersed phase and (*d*) the carrier phase for a case with the same Ga ($= 7$) and two different values of Bo to examine the effect of bubble deformation on the gas transfer.

$Pe = u_b r_0/D_c = \sqrt{gr_0}r_0/D_c$; the data show a consistent increased time to saturation as the Péclet number increases.

Finally, we wish to evaluate the contribution of the bubble deformability to the mass transfer. To this end, we increase the Bond number from 0.08 to 0.3 (i.e. reduce the surface tension) while keeping the other parameters constant, in particular, $Ga = 7$, $\alpha = 1.9\,\%$ and $Sc = 10$. The results depicted in figures 11(*c*) and 11(*d*) show that the mass transfer is independent of Bo when this is below unity, i.e. when the bubble shape can be considered as nearly spherical. Increasing Bo to values larger than unity leads to merging and coalescence and it is therefore not considered in this study. Future work may be devoted to deformable bubbles with merging/coalescence and the effect of surfactants. Thus, for the ranges of bubble sizes considered in this study, the difference in species transfer is attributed to the rising speed, via Ga, and not to deformability, i.e. to the Bond number Bo. Note that for the cases considered in this study the average bubble deformation is 0.98, which indicates that the bubbles experience limited deformation due to the low values of the Bond number.

https://doi.org/10.1017/jfm.2026.11338 Published online by Cambridge University Press

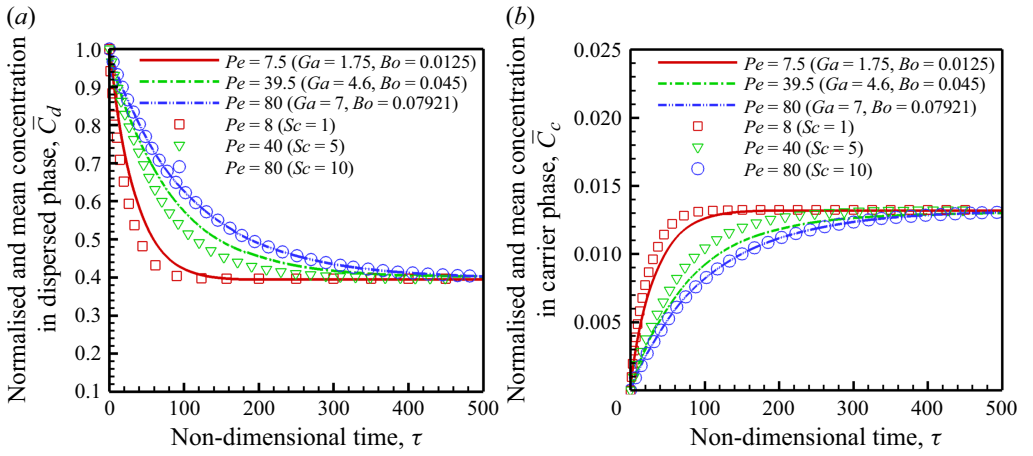


Figure 12. Time evolution of the normalised and averaged species concentration in (*a*) the dispersed phase and (*b*) the carrier phase for varying bubble sizes and Schmidt number Sc, at a constant void fraction $\alpha = 1.9\,\%$. The species transfer evolution is adapted from figure 8 for varying Sc and figure 11 for different bubble sizes. For each case we also report the value of the Péclet number $Pe = \sqrt{gr_0}r_0/D_c$.

4.3. *A phenomenological model*

To gain insight into the mechanisms of the species dissolution from multiple rising bubbles in a liquid carrier phase, we derive a mass transfer model able to predict the numerical data discussed in the previous section. Therefore, the objectives of this section are: first, to propose a physically sound yet simple model to describe the mass transfer resulting from the complex interactions between buoyancy-driven bubbles and the surrounding carrier phase; second, to find suitable scaling parameters for the variation in species transfer with Sc, Ga and α.

Using data from an experiment of bubbly flow with void fraction α in the range $1.46\,\%-26.9\,\%$, Colombet *et al.* (2015) related the rate of variation of dissolved oxygen concentration with void fraction, α, the volume-averaged interfacial area, $a_{\Gamma(\phi)}$, and an effective mass transfer coefficient, k_c. Thus, let us also start with the equation for the rate of change of the mean species concentration in the carrier phase:

$$\frac{\partial \overline{C}_c}{\partial t} = \frac{k_c a_{\Gamma(\phi)}}{(1-\alpha)}\left(\overline{C}_{c,\Gamma(\phi)} - \overline{C}_{c,\infty}\right), \tag{4.2}$$

where the subscripts 'Γ' and '∞' denote the carrier-side species concentration at the interface and far from the interface.

The volume-averaged interfacial area $a_{\Gamma(\phi)}$ is related to the void fraction α by

$$a_{\Gamma(\phi)} = f\frac{\Sigma_1^{N_b} S_{\Gamma(\phi)}}{\Sigma_1^{N_b} V_b} \quad \text{and} \quad \alpha = \frac{\Sigma_1^{N_b} V_b}{V_{cd}}, \tag{4.3}$$

where $S_{\Gamma(\phi)}$ and V_b are the interfacial area and the volume of a single bubble, N_b the total number of bubbles inside the computational domain and V_{cd} the total volume of the computational domain (taking the latter as our control volume). In this study, we have considered relatively low values of the Bond number Bo so that the bubble deformation is minimum and there are no bubble–bubble interactions as shown in figure 4. Hence, assuming a constant number of bubbles of spherical shape, the volume-averaged interfacial

https://doi.org/10.1017/jfm.2026.11338 Published online by Cambridge University Press

area $a_{\Gamma(\phi)}$ can be written in terms of the void fraction and the bubble size as

$$a_{\Gamma(\phi)} = \alpha \frac{3}{r_0}, \tag{4.4}$$

where r_0 is the initial bubble radius which remains constant due to negligible bubble deformation (low Bo), the assumption of no volume shrinkage (dilute conditions for the species undergoing mass transfer) and the absence of coalescence.

Let us now estimate the mass transfer coefficient as the ratio of species diffusivity in the carrier phase D_c to the scalar boundary-layer thickness δ_c:

$$k_c \sim \frac{D_c}{\delta_c}. \tag{4.5}$$

To motivate the choice the reader is referred to Nellis & Klein (2008) and the recent study of heated drops or bubbles in turbulent channel flows by Mangani *et al.* (2024) who, similarly, estimated the heat transfer coefficient as the ratio of the thermal conductivity of the carrier phase to the thermal boundary-layer thickness. Further, assuming a uniform species distribution within bubbles due to the relatively low Schmidt number in the dispersed phase, the concentration difference in (4.2) is approximated as

$$\left(\overline{C}_{c,\Gamma(\phi)} - \overline{C}_{c,\infty}\right) \approx \left(H_e \overline{C}_{d,\Gamma(\phi)} - \overline{C}_{c,\infty}\right) \approx \left(H_e \overline{C}_d - \overline{C}_{c,\infty}\right), \tag{4.6}$$

where H_e is Henry's coefficient and the subscripts $(c, \Gamma(\phi))$ and $(d, \Gamma(\phi))$ denote the carrier-side and dispersed-side species concentrations at the interface. To estimate the ratio between the boundary-layer thicknesses, Weiner & Bothe (2017) proposed a relationship between the average concentration boundary-layer thickness δ_c and the average hydrodynamic boundary-layer thickness δ_v for a rising single bubble via the carrier-phase Schmidt number, Sc_c, as $\delta_c \propto \delta_v Sc_c^{-1/2}$. See figure 1($f$) which shows that this expected scaling is obtained from our simulations of a single rising bubble. For the more general case of multiple bubbles, considering more complex flow conditions near the bubble interface, the scaling of δ_c can be expressed as

$$\delta_c \propto \delta_v Sc_c^{-\beta}. \tag{4.7}$$

A similar scaling is adopted for the thermal boundary-layer thickness, $\delta_c \propto \delta_v Pr_c^{-\alpha}$, in Mangani *et al.* (2024), where Pr is the Prandtl number.

Considering the initial bubble radius r_0 as length scale l_c, the characteristic velocity scale denoted as u_c, the convective time as characteristic time scale t_c $(= l_c/u_c)$ and the saturation concentration in the carrier phase $c_{sat,c}$, we obtain the non-dimensional form of (4.2); substituting the expressions (4.5)–(4.7) in (4.2) we finally write

$$\frac{\partial \tilde{C}_c}{\partial \tau} = \left(\frac{D_c}{\delta_v Sc_c^{-\beta}}\right)\left(\frac{3\alpha}{r_0(1-\alpha)}\right)\left(\frac{r_0}{u_c}\right)\left(H_e \tilde{C}_d - \tilde{C}_c\right), \tag{4.8}$$

where we have approximated the far-field concentration with the mean concentration in the carrier phase $(\overline{C}_c \approx \overline{C}_{c,\infty})$. Note that, alternatively, a diffusive time scale may be utilised; however, in that case, the corresponding non-dimensionalisation would involve multiplication by the Péclet number.

Further rearranging the above terms and expressing the velocity scale as $u_c = \sqrt{gr_0}$, we obtain the following non-dimensional expression:

$$\frac{\partial \tilde{C}_c}{\partial \tau} = \frac{3}{\tilde{\delta}_v(1-\alpha)} \alpha Sc^{-1+\beta} Ga^{-1}\left(H_e \tilde{C}_d - \tilde{C}_c\right), \tag{4.9}$$

https://doi.org/10.1017/jfm.2026.11338 Published online by Cambridge University Press

where τ, $A_{\Gamma(\phi)}$, $\tilde{\delta}_v$ and $\tilde{C}$ are the non-dimensional time, volume-averaged interfacial area, velocity boundary-layer thickness and concentration. Rewriting the above equation in terms of a flow-dependent constant $C = 3/\tilde{\delta}_v$ and approximating $1-\alpha \approx 1$ because of the low void fractions considered in this study results in the following simplified form of (4.9):

$$\frac{\partial \tilde{C}_c}{\partial \tau} = C\alpha Sc^{-1+\beta} Ga^{-1}\left(H_e \tilde{C}_d - \tilde{C}_c\right). \tag{4.10}$$

In the experiment by Gvozdić *et al.* (2018) with rising air bubbles in water of equivalent radius 1.28 mm and void fractions in the range 0.5 %−1.05 %, the velocity fluctuations in the carrier phase are found to scale as $\alpha^{0.4}$, so that we can rewrite the flow-dependent coefficient as

$$C \sim K\alpha^{-\gamma}, \tag{4.11}$$

where K is a constant which solely depends on the velocity boundary-layer characteristics and a negative exponent is assumed because of the inverse relation to $\tilde{\delta}_v$ in (4.9). Assuming $\lambda = 1-\gamma$, (4.10) thus reduces to

$$\frac{\partial \tilde{C}_c}{\partial \tau} = K\alpha^{\lambda} Sc^{-1+\beta} Ga^{-1}\left(H_e \tilde{C}_d - \tilde{C}_c\right). \tag{4.12}$$

Equation (4.12) can be numerically integrated to compute the mean species concentration in the carrier phase. Two factors need to be evaluated to actually solve the equation: β and γ. The exponent β is evaluated here based on previous studies on the boundary-layer scaling for heat and mass transfer. As mentioned above, the species boundary-layer thickness (δ_c) is assumed to scale with the velocity boundary-layer thickness (δ_v) and the Schmidt number (Sc) as $\delta_c \sim \delta_v Sc^{-\beta}$ (Levich 1962; Clift, Grace & Weber 1978; Weiner & Bothe 2017). A similar scaling is also reported for the thermal boundary-layer thickness (δ_t) as $\delta_t \sim \delta_v Pr^{-\beta}$ (Schlichting & Gersten 2016), Pr being the Prandtl number. The exponent β is found to be $1/3$ for no-slip interface conditions, e.g. solid particles, and $1/2$ for free-slip conditions, more relevant to bubbles (Bird 2002; Nellis & Klein 2008). Note, however, that in a recent numerical study on species transfer, surface contaminants are found to strongly dampen the velocity fluctuations resulting in a better accuracy when assuming a no-slip surface condition rather than a free-slip condition (Herlina & Wissink 2016). This approximation gives a scaling of the species effective diffusion in the carrier phase as $Sc^{-2/3}$ for a contaminated surface. For clean surfaces the scaling for effective diffusion changes to $Sc^{-1/2}$. Thus, in general, the hydrodynamic and interface conditions control the effective species diffusion in the carrier phase, which scales with Sc^{η} (Herlina & Wissink 2016), with typically the factor η varying from $-1/2$ for free-slip condition to $-2/3$ for no-slip condition (Jähne & Haußecker 1998). Note also that, from (4.12), $\eta = -1+\beta$.

To determine the factor γ in (4.12), we exploit the analogy between the species and temperature transport as passive scalars in bubbly flows. The recent study by Gvozdić *et al.* (2018) for heat transfer in bubbly flows demonstrated the prevalence of bubble-induced diffusion over natural convection resulting in a scaling of the Nusselt number, $Nu \sim \alpha^{\lambda}$. For void fractions $\alpha = 0\,\%-5\,\%$, the exponent $\lambda = 0.45$ was found to better approximate the data (see Gvozdić *et al.* 2018). A similar diffusion-dominated process is also reported for mixing of a passive scalar at low void fractions, $\alpha < 1\,\%$, and in the transitional regime $1\,\% \leqslant \alpha \leqslant 3\,\%$ (see Alméras *et al.* 2015, 2019). Assuming an analogous behaviour for our problem of species transfer, we take $\lambda\ (= 1-\gamma) = 0.45$ for the model in (4.12).

https://doi.org/10.1017/jfm.2026.11338 Published online by Cambridge University Press

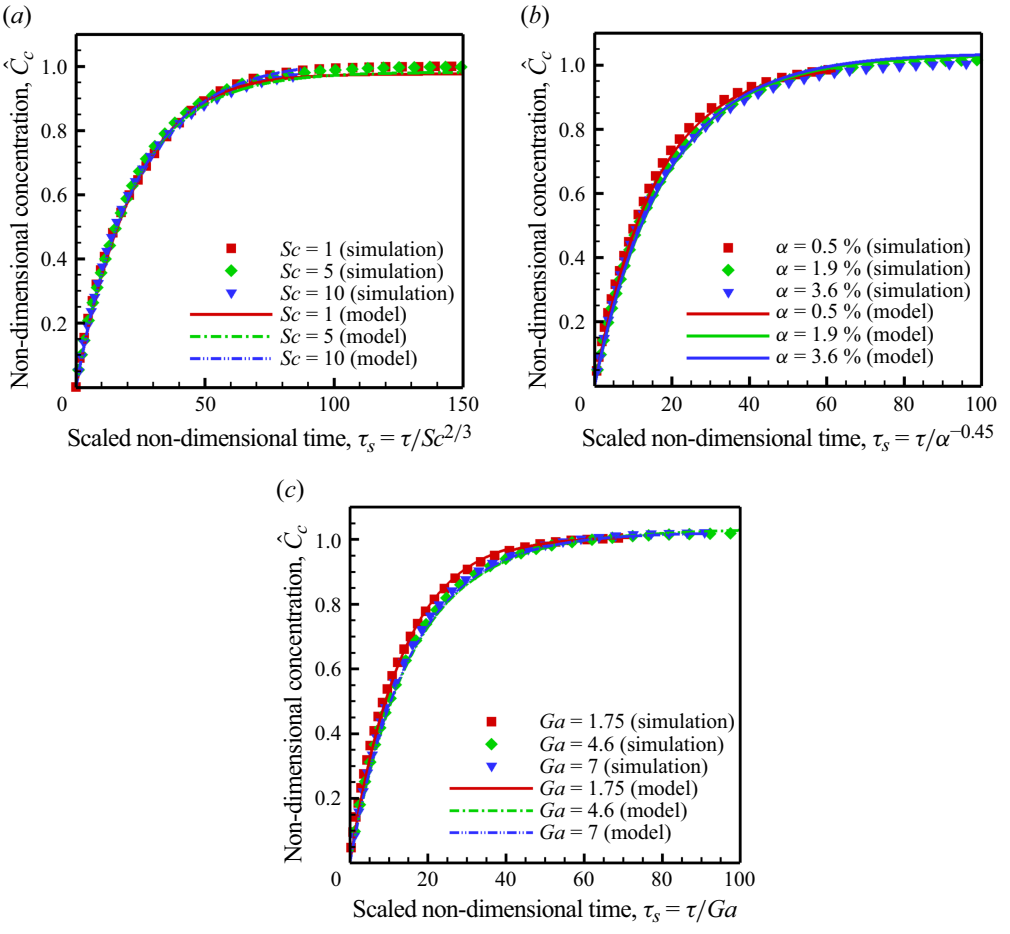


Figure 13. Comparison between the simulation data and the results of the proposed model; see (4.12) in the text. The figure also documents the self-similar characteristics of the temporal evolution of the non-dimensional species concentration in the carrier phase when utilising a suitably scaled non-dimensional time (see discussion in the text) when varying (*a*) the Schmidt number, (*b*) the void fraction and (*c*) the bubble size.

We now compare the predictions from the proposed phenomenological model in (4.12) with the results of the interface-resolved simulations. The agreement when examining the time evolution of the average species concentration is excellent with the values $\eta = -2/3$ and $\lambda = 0.45$ as shown in figure 13. As introduced above, the value $\eta = -2/3$ denotes the predominance of diffusion over advection close to the interfaces ($\beta = 1/3$ for a no-slip condition). Even though clean bubbles are considered in the simulations, i.e. without any surface contaminants and Marangoni stresses, the scaling $Sc^{2/3}$ could be attributed to weak convective effects at the interface due to the small bubble size ($r_0 < 1$ mm) considered in this study (see also the discussion in Scarbolo & Soldati (2013) about the weakening of convective effects induced by the bubble interface). For a single bubble or a very sparse bubble population, convective effects further decrease, leading to a stronger relative contribution from diffusion. A similar trend is also reported by Mangani *et al.* (2024) who report a scaling with $Pr^{2/3}$ during the initial stages of their simulation when drops or bubbles are also small. Note that once coalescence has modified the size

https://doi.org/10.1017/jfm.2026.11338 Published online by Cambridge University Press

distribution, their scaling changes to $Pr^{1/2}$. Our study shows that a similar weakening is found also when the viscosity and density contrasts are relevant.

The choice of the exponent $\lambda = 0.45$, which indicates the increase of gas transfer with α, follows the observations for the cases of mixing in a homogeneous bubbly flow at low void fractions ($\alpha = 0.5\,\%,\ 1.9\,\%$ and $3.6\,\%$) in Alméras *et al.* (2015). Here, we relate this increase to the increase in velocity fluctuations with the void fraction. Our numerical results present an increase of the velocity fluctuations with void fraction proportional to $\alpha^{0.35}$, in agreement with experiments at void fractions of $1\,\%-13\,\%$ and equivalent air bubble radii between 0.8 and 1.95 mm in water, where the velocity fluctuations were found to scale as $\alpha^{0.4}$ (Riboux *et al.* 2010; Alméras *et al.* 2015). The scaling with $\lambda = 0.45$ for the species transfer therefore suggests an enhanced contribution from bubble-induced mixing combined with the increase in interfacial area. Note that no coalescence was observed for the current bubble configuration up to a void fraction of 4 %, and the model can be applied within this range. For higher void fractions, where bubble coalescence begins to occur, a bubble-size-distribution-based extension of the model would be required.

As directly suggested by the model in (4.12), a good agreement between model and simulation is obtained by scaling time with $Sc^{2/3}$, $\alpha^{-0.45}$ and Ga as shown in figure 13(*a–c*) for varying values of Sc, α and Ga. We finally note that the linear scaling of species transfer with Ga, along with the independence of velocity fluctuations from Ga, suggests a scaling of the mass transfer with the bubble rising velocity.

Finally, since the rate of change of mean species concentration in the carrier phase predicted by our model in (4.12) shows good agreement with the simulation data (see figure 13), a unique scaling parameter for the non-dimensional time (τ) is considered:

$$\tau_s^+ = \frac{\tau}{\left(\dfrac{Sc^{2/3}Ga}{\alpha^{0.45}}\right)}, \tag{4.13}$$

where τ_s^+ is the rescaled non-dimensional time. On plotting the time evolution of the species concentration in the carrier phase for all cases considered in this study versus the non-dimensional time (τ_s^+), all curves collapse onto a master curve, as shown in figure 14. This demonstrates the self-similar characteristics of the non-dimensional species concentration in the carrier phase when different governing parameters are varied – Schmidt number, void fraction and bubble size – for the range considered in this study.

5. Conclusions

Using a CDI-based in-house multiphase solver, we have performed numerical simulations of the mass transfer of a dilute species from multiple rising bubbles in a carrier liquid phase. In particular, we have investigated the transient behaviour of the species transfer and the evolution of the volume-averaged scalar concentration in the dispersed and carrier phases while varying some of the input parameters: Schmidt number (Sc), bubble size and void fraction (α). Our representative volume consists of 12 bubbles, as suggested by previous numerical studies of bubbly flow. As regards the flow dynamics, the bubbles are initialised with random initial position, at large enough distance from each other to avoid their merging. For the mass transfer, we specify a constant uniform species concentration throughout the dispersed phase and zero in the liquid at the start of the numerical experiments. For this configuration, each of the input parameters above is varied while keeping the other two constant.

https://doi.org/10.1017/jfm.2026.11338 Published online by Cambridge University Press

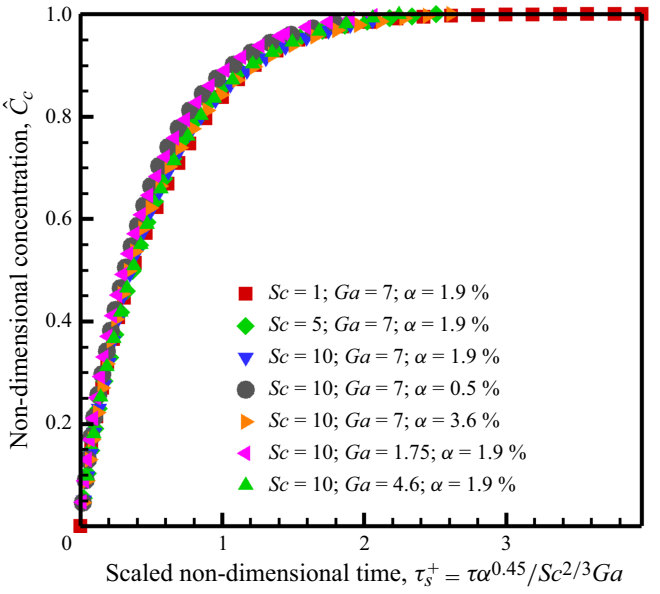


Figure 14. Scaling of non-dimensional time τ with $(Sc^{2/3}Ga/\alpha^{0.45})$ for the different flow configurations simulated in this study. The data pertaining to the average scalar concentration in the carrier phase nearly collapse to a master curve.

The increase in Sc obtained by reducing the species diffusivity while keeping the ratio between diffusivity in carrier and dispersed phase constant results in an increase of the time needed for saturation, with the time to saturation scaling as $Sc^{2/3}$. A similar trend is observed with variations in the bubble size: the concentration in the carrier phase reaches a similar saturation value, but the time taken for saturation decreases with an increase in bubble size due to increased convective effects. The time to saturation is found to scale with Ga, a non-dimensional measure of the bubble rising speed versus viscous diffusion. Considering together the variations in diffusivity and bubble size, we show that the mass transfer rate and the time to saturation can be well represented by a Péclet number $Pe = \sqrt{gr_0}r_0/D_c$ based on the bubble rising speed, its radius and the species diffusivity. Note that the increase in bubble size, and consequently of the rising speed, implies an increase of the Galilei number and of the Bond number, which can be related to the bubble deformability. However, for the values of bubble radii and surface tension considered here, deformations are limited and the dispersed bubbles retain their spherical shape, which explains why the mass transfer rate is found to be only a function of the Galilei number.

Finally, we have considered variation of the void fraction, α, in the range 0.5 %–3.6 %. This not only changes the final saturation concentration, but also the transfer rate. This is found to initially increase with the void fraction because of the largest interfacial area (see early time evolution in figure 9*b*) and then decrease once the scalar concentration wakes and boundary layer start to interact. Note also that the fluid velocity fluctuations increase in the carrier phase when increasing the void fraction, which further contributes to the mixing and to the initial mass transfer rate. Because of the combined effect of more interfacial area and increased velocity fluctuations, we observe an almost linear scaling of transfer rate with void fraction, $\sim\alpha^{0.9}$, larger than the only increase of the surface area ($\sim\alpha^{2/3}$). As a consequence of this complex nonlinear interplay between interfacial fluxes and flow

https://doi.org/10.1017/jfm.2026.11338 Published online by Cambridge University Press

mixing, an empirical exponent needs to be estimated for the mass transfer dependence on the void fraction.

Here, we also propose a phenomenological model able to predict the temporal evolution of the mean species concentration as function of the different input parameters, similar to the recent phenomenological model for heat transfer with different Prandtl number in Mangani *et al.* (2024). The model assumes that, for the relatively small bubbles considered here, the species boundary-layer thickness scales with the Schmidt number as $Sc^{1/3}$; a scaling also reported by Mangani *et al.* (2024) for the behaviour of the thermal boundary-layer thickness with the Prandtl number, $\delta_T \sim Pr^{1/3}$. Moreover, the model is based on a flow-structure-dependent parameter, mimicking the mixing in the multiphase flow, which is found to scale with the void fraction as $\alpha^{0.45}$, in agreement with previous studies on bubbly flows (Riboux *et al.* 2010; Alméras *et al.* 2015).

Overall, this results in the rate of species transfer being dependent on $Sc^{-2/3}$, $\alpha^{0.45}$ and Ga^{-1}. Hence, a self-similar behaviour of the mass transfer is demonstrated when scaling the non-dimensional time with $(Sc^{2/3}Ga/\alpha^{0.45})$, resulting in a collapse of the data for the mean average concentration on a master curve for the parameter range of this study. The self-similar time evolution is provided by the solution of (4.12).

This study therefore demonstrates the transient evolution of species transfer and proposes a phenomenological model to predict the transient characteristics of the process, adding to previous studies based on the time-averaged behaviour of species transfer. This work can therefore be extended in a number of non-trivial ways. As example, we believe it would be interesting to consider regimes where bubble deformation, coalescence or breakup may impact the dynamics described here, as well as to consider configurations characterised by self-sustained background turbulence.

Acknowledgements. The computations were performed on resources provided by Sigma2 – the National Infrastructure for High-Performance Computing and Data Storage in Norway with project number NN9646K.

Funding. The work was supported by the Research Council of Norway (NRC) (grant no. 334652).

Declaration of interests. The authors report no conflict of interest.

Data availability statement. Data are available on request from the authors.

Appendix. Sensitivity of the phenomenological model to the exponent of the void fraction

To determine the robustness of the phenomenological model introduced in § 4.3, we evaluate the sensitivity of the exponent utilised for the role of the void fraction α. To this end, we vary the exponent between the limits reported in the literature for bubbly flows (Riboux *et al.* 2010; Alméras *et al.* 2015), i.e. between 0.40 and 0.50 in increments of 0.01. For each of the different scenarios with varying Schmidt number (Sc), bubble size (r_0) and void fraction (α), the exponent is varied within the chosen range and the spatially averaged concentration is calculated. For comparison, the relative percentage error between the phenomenological model and the corresponding simulation is computed as shown in figure 15. In every case, the relative error decreases monotonically as the exponent is increased from 0.40 and attains a minimum near the value of 0.45 (relative error $\approx$2 %), and increases again for $\lambda > 0.45$; see figures 15(*a*)–15(*c*) for the flow cases with different Sc, r_0 and α, respectively. Thus, the location of the minimum remains nearly unchanged across the different cases. Overall, the analysis confirms that the model is both robust and predictive for the chosen exponent.

https://doi.org/10.1017/jfm.2026.11338 Published online by Cambridge University Press

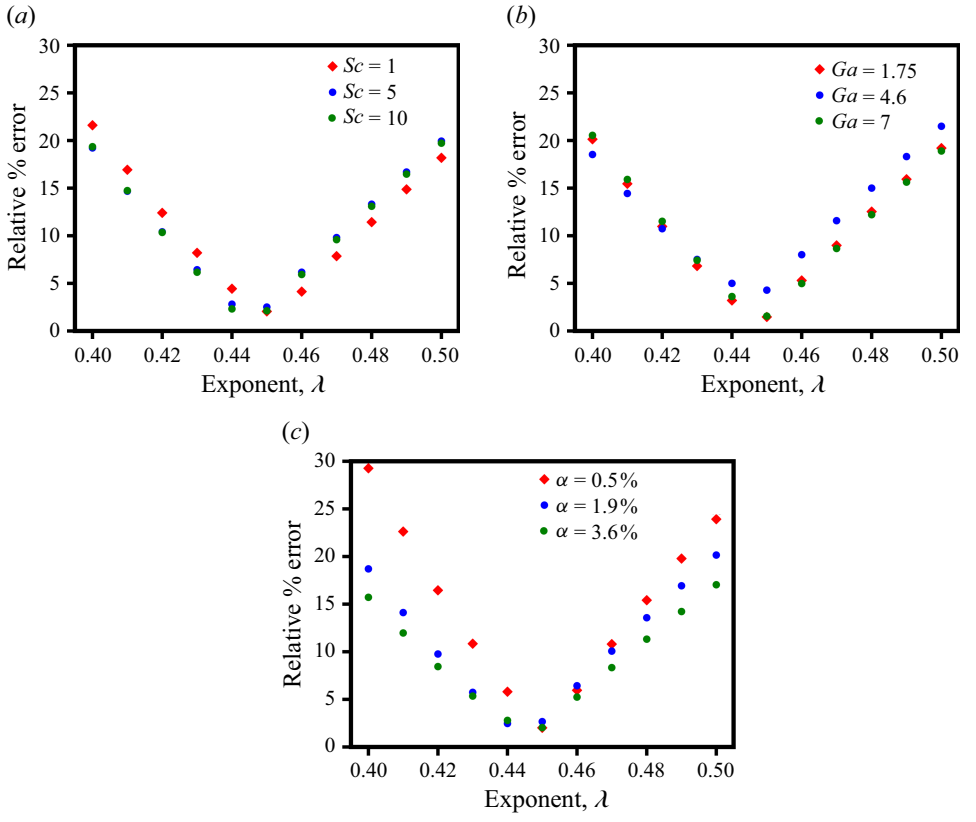


Figure 15. Variation of relative percentage error with the exponent λ in the phenomenological model (4.12) for different (*a*) Schmidt numbers, (*b*) bubble sizes and (*c*) void fractions.

References

Aboulhasanzadeh, B., Hosoda, S., Tomiyama, A. & Tryggvason, G. 2013 A validation of an embedded analytical description approach for the computations of high Schmidt number mass transfer from bubbles in liquids. *Chem. Engng Sci.* **101**, 165–174.

Aboulhasanzadeh, B., Thomas, S., Taeibi-Rahni, M. & Tryggvason, G. 2012 Multiscale computations of mass transfer from buoyant bubbles. *Chem. Engng Sci.* **75**, 456–467.

Aboulhasanzadeh, B. & Tryggvason, G. 2014 Effect of bubble interactions on mass transfer in bubbly flow. *Intl J. Heat Mass Transfer* **79**, 390–396.

Ahmed, Z., Izbassarov, D., Costa, P., Muradoglu, M. & Tammisola, O. 2020 Turbulent bubbly channel flows: effects of soluble surfactant and viscoelasticity. *Comput. Fluids* **212**, 104717.

Alméras, E., Mathai, V., Sun, C. & Lohse, D. 2019 Mixing induced by a bubble swarm rising through incident turbulence. *Intl J. Multiphase Flow* **114**, 316–322.

Alméras, E., Risso, F., Roig, V., Cazin, S., Plais, C. & Augier, F. 2015 Mixing by bubble-induced turbulence. *J. Fluid Mech.* **776**, 458–474.

Balcázar-Arciniega, N., Antepara, O., Rigola, J. & Oliva, A. 2019 A level-set model for mass transfer in bubbly flows. *Intl J. Heat Mass Transfer* **138**, 335–356.

Balcázar-Arciniega, N., Rigola, J., Pérez-Segarra, C.D. & Oliva, A. 2024 Numerical study of the drag force, interfacial area and mass transfer in bubbles in a vertical pipe. *Chem. Engng J.* **495**, 153124.

Bhuvankar, P. & Dabiri, S. 2018 Impact of a single bubble rising near a wall on the wall-to-liquid heat flux. *Intl J. Heat Mass Transfer* **116**, 445–457.

Bird, R.B. 2002 Transport phenomena. *Appl. Mech. Rev.* **55** (1), R1–R4.

Bothe, D. & Fleckenstein, S. 2013 A Volume-of-Fluid-based method for mass transfer processes at fluid particles. *Chem. Engng Sci.* **101**, 283–302.

https://doi.org/10.1017/jfm.2026.11338 Published online by Cambridge University Press

BUNNER, B. & TRYGGVASON, G. 1999 An examination of the flow induced by the motion of many buoyant bubbles. *J. Vis.* **2** (2), 153–158.
BUNNER, B. & TRYGGVASON, G. 2002*a* Dynamics of homogeneous bubbly flows. Part 1. Rise velocity and microstructure of the bubbles. *J. Fluid Mech.* **466**, 17–52.
BUNNER, B. & TRYGGVASON, G. 2002*b* Dynamics of homogeneous bubbly flows. Part 2. Velocity fluctuations. *J. Fluid Mech.* **466**, 53–84.
BUNNER, B. & TRYGGVASON, G. 2003 Effect of bubble deformation on the properties of bubbly flows. *J. Fluid Mech.* **495**, 77–118.
CHAI, S.Y.W., NGU, L.H. & HOW, B.S. 2022 Review of carbon capture absorbents for CO_2 utilization. *Greenh. Gases Sci. Technol.* **12** (3), 394–427.
CHIRAMMEL, S.S., SHARMA, A. & MURALLIDHARAN, J.S. 2023 On ghost fluid method-based sharp interface level set method on a co-located grid and its comparison with balanced force-based diffuse interface method. *J. Comput. Phys.* **485**, 112109.
CLIFT, R., GRACE, J.R. & WEBER, M.E. 1978 *Bubbles, Drops, and Particles*, 2nd edn. Dover Publications.
COLOMBET, D., LEGENDRE, D., COCKX, A., GUIRAUD, P., RISSO, F., DANIEL, C. & GALINAT, S. 2011 Experimental study of mass transfer in a dense bubble swarm. *Chem. Engng Sci.* **66** (14), 3432–3440.
COLOMBET, D., LEGENDRE, D., RISSO, F., COCKX, A. & GUIRAUD, P. 2015 Dynamics and mass transfer of rising bubbles in a homogenous swarm at large gas volume fraction. *J. Fluid Mech.* **763**, 254–285.
CRANK, J. 1975 *The Mathematics of Diffusion*. Clarendon Press.
DABIRI, S., LU, J. & TRYGGVASON, G. 2013 Transition between regimes of a vertical channel bubbly upflow due to bubble deformability. *Phys. Fluids* **25** (10), 102110.
DEEN, N.G. & KUIPERS, J.A.M. 2013 Direct numerical simulation of wall-to liquid heat transfer in dispersed gas–liquid two-phase flow using a volume of fluid approach. *Chem. Engng Sci.* **102**, 268–282.
DORAN, P.M. 2013 *Bioprocess Engineering Principles*, 2nd edn. Academic Press.
ESMAEELI, A. & TRYGGVASON, G. 1996 An inverse energy cascade in two-dimensional low Reynolds number bubbly flows. *J. Fluid Mech.* **314**, 315–330.
ESMAEELI, A. & TRYGGVASON, G. 1998 Direct numerical simulations of bubbly flows. Part 1. Low Reynolds number arrays. *J. Fluid Mech.* **377**, 313–345.
ESMAEELI, A. & TRYGGVASON, G. 1999 Direct numerical simulations of bubbly flows. Part 2. Moderate Reynolds number arrays. *J. Fluid Mech.* **385**, 325–358.
ESMAEELI, A. & TRYGGVASON, G. 2005 A direct numerical simulation study of the buoyant rise of bubbles at O(100) Reynolds number. *Phys. Fluids* **17** (9), 093303.
FARSOIYA, P.K., MAGDELAINE, Q., ANTKOWIAK, A., POPINET, S. & DEIKE, L. 2023 Direct numerical simulations of bubble-mediated gas transfer and dissolution in quiescent and turbulent flows. *J. Fluid Mech.* **954**, A29.
FENG, X., YANG, C., MAO, Z.-S., LU, J. & TRYGGVASON, G. 2019 Bubble induced turbulence model improved by direct numerical simulation of bubbly flow. *Chem. Engng J.* **377**, 120001.
FIGUEROA-ESPINOZA, B. & ZENIT, R. 2005 Clustering in high Re monodispersed bubbly flows. *Phys. Fluids* **17** (9), 091701.
GVOZDIĆ, B., ALMÉRAS, E., MATHAI, V., ZHU, X., VAN GILS, D.P.M., VERZICCO, R. & LOHSE, D. 2018 Experimental investigation of heat transport in homogeneous bubbly flow. *J. Fluid Mech.* **845**, 226–244.
GÖZ, M.F., BUNNER, B., SOMMERFELD, M. & TRYGGVASON, G. 2000 The unsteady dynamics of two-dimensional bubbles in a regular array. In *Proceedings of ASME FEDSM00 Fluids Engineering Division Summer Meeting, Boston, MA*, pp. 11–15.
GÖZ, M.F., SOMMERFELD, M., BUNNER, B. & TRYGGVASON, G. 2002 Microstructure of a bidisperse swarm of spherical bubbles. In *The Proceedings of the ASME Joint U.S.-European Fluids Engineering Division Conference, Montreal, QC, Canada*, vol. 2, pp. 549–555.
HERLINA, H. & WISSINK, J.G. 2016 Isotropic-turbulence-induced mass transfer across a severely contaminated water surface. *J. Fluid Mech.* **797**, 665–682.
ISHII, M. & HIBIKI, T. 2010 *Thermo-Fluid Dynamics of Two-Phase Flow*. Springer Science & Business Media.
JAIN, S.S. & MANI, A. 2020 Modeling transport of scalars in two-phase flows with a diffuse-interface method. ArXiv preprint arXiv: 2011.10705.
JIN, Y., CAVERO, R.F., WEILAND, C., HOFFMANN, M. & SCHLÜTER, M. 2023 Effects of bubble-induced turbulence on interfacial species transport: a direct numerical simulation study. *Chem. Engng Sci.* **279**, 118934.
JIN, Y. & SCHLÜTER, M. 2019 Direct numerical simulation of the interfacial mass transfer of a bubble in self-induced turbulent flows. *Intl J. Heat Mass Transfer* **135**, 1248–1259.
JÄHNE, B. & HAUSSECKER, H. 1998 Air–water gas exchange. *Annu. Rev. Fluid Mech.* **30**, 443–468.

https://doi.org/10.1017/jfm.2026.11338 Published online by Cambridge University Press

KURE, I.K., JAKOBSEN, H.A. & SOLSVIK, J. 2023 Interface mass transfer and properties of bubbly flows in a column with Newtonian and non-Newtonian liquids. *Chem. Engng Sci.* **277**, 118828.
LEVICH, F.G. 1962 *Physicochemical Hydrodynamics*, 1st edn. Prentice-Hall.
LIN, S., LU, J., TRYGGVASON, G. & ZHANG, Y. 2018 A numerical study of oscillation induced coalescence in bubbly flows. *Phys. Fluids* **30** (12), 127105.
LIN, S., LU, J., TRYGGVASON, G. & ZHANG, Y. 2019 The effect of fluid shear on oscillating bubbly flows. *Phys. Fluids* **31** (4), 042110.
LOISY, A., NASO, A. & SPELT, P.D.M. 2017 Buoyancy-driven bubbly flows: ordered and free rise at small and intermediate volume fraction. *J. Fluid Mech.* **816**, 94–141.
LOISY, A., NASO, A. & SPELT, P.D.M. 2018 The effective diffusivity of ordered and freely evolving bubbly suspensions. *J. Fluid Mech.* **840**, 215–237.
LU, J., MURADOGLU, M. & TRYGGVASON, G. 2017 Effect of insoluble surfactant on turbulent bubbly flows in vertical channels. *Intl J. Multiphase Flow* **95**, 135–143.
LU, J. & TRYGGVASON, G. 2006 Numerical study of turbulent bubbly downflows in a vertical channel. *Phys. Fluids* **18** (10), 103302.
LU, J. & TRYGGVASON, G. 2008 Effect of bubble deformability in turbulent bubbly upflow in a vertical channel. *Phys. Fluids* **20** (4), 040701.
MA, T., LUCAS, D., JAKIRLIĆ, S. & FRÖHLICH, J. 2020 Progress in the second-moment closure for bubbly flow based on direct numerical simulation data. *J. Fluid Mech.* **883**, A9.
MA, T., SANTARELLI, C., ZIEGENHEIN, T., LUCAS, D. & FRÖHLICH, J. 2017 Direct numerical simulation–based Reynolds-averaged closure for bubble-induced turbulence. *Phys. Rev. Fluids* **2** (3), 034301.
MANGANI, F., ROCCON, A., ZONTA, F. & SOLDATI, A. 2024 Heat transfer in drop-laden turbulence. *J. Fluid Mech.* **978**, A12.
MEZUI, Y., OBLIGADO, M. & CARTELLIER, A. 2023 Buoyancy-driven bubbly flows: role of meso-scale structures on the relative motion between phases in bubble columns operated in the heterogeneous regime. *J. Fluid Mech.* **962**, A40.
MIRJALILI, S., IVEY, C.B. & MANI, A. 2020 A conservative diffuse interface method for two-phase flows with provable boundedness properties. *J. Comput. Phys.* **401**, 109006.
MIRJALILI, S., JAIN, S.S. & MANI, A. 2022 A computational model for interfacial heat and mass transfer in two-phase flows using a phase field method. *Intl J. Heat Mass Transfer* **197**, 123326.
MURAI, Y., SONG, X.Q., TAKAGI, T., ISHIKAWA, M.A., YAMAMOTO, F. & OHTA, J. 2000 Inverse energy cascade structure of turbulence in a bubbly flow: PIV measurement and results. *JSME Intl J. Ser. B* **43** (2), 188–196.
NELLIS, G. & KLEIN, S. 2008 *Heat Transfer*. Cambridge University Press.
NEMATI, H., BREUGEM, W.-P., KWAKKEL, M. & BOERSMA, B.J. 2021 Direct numerical simulation of turbulent bubbly down flow using an efficient CLSVOF method. *Intl J. Multiphase Flow* **135**, 103500.
PANDA, A., WEITKAMP, Y.E.J., RAJKOTWALA, A.H., PETERS, E.A.J.F., BALTUSSEN, M.W. & KUIPERS, J.A.M. 2019 Influence of gas fraction on wall-to-liquid heat transfer in dense bubbly flows. *Chem. Engng Sci. X* **4**, 100037.
PASHAEI, H., ZARANDI, M.N. & GHAEMI, A. 2017 Experimental study and modeling of CO_2 absorption into diethanolamine solutions using stirrer bubble column. *Chem. Engng Res. Des.* **121**, 32–43.
PIEDRA, S., LU, J., RAMOS, E. & TRYGGVASON, G. 2015 Numerical study of the flow and heat transfer of bubbly flows in inclined channels. *Intl J. Heat Fluid Flow* **56**, 43–50.
RHIE, C.M. & CHOW, W.L. 1983 Numerical study of the turbulent flow past an airfoil with trailing edge separation. *AIAA J.* **21** (11), 1525–1532.
RIBOUX, G., RISSO, F. & LEGENDRE, D. 2010 Experimental characterization of the agitation generated by bubbles rising at high Reynolds number. *J. Fluid Mech.* **643**, 509–539.
RISSO, F. & ELLINGSEN, K. 2002 Velocity fluctuations in a homogeneous dilute dispersion of high-Reynolds-number rising bubbles. *J. Fluid Mech.* **453**, 395–410.
ROGHAIR, I., BALTUSSEN, M.W., VAN SINT ANNALAND, M. & KUIPERS, J.A.M. 2013 Direct numerical simulations of the drag force of bi-disperse bubble swarms. *Chem. Engng Sci.* **95**, 48–53.
ROGHAIR, I., LAU, Y.M., DEEN, N.G., SLAGTER, H.M., BALTUSSEN, M.W., VAN SINT ANNALAND, M. & KUIPERS, J.A.M. 2011 On the drag force of bubbles in bubble swarms at intermediate and high Reynolds numbers. *Chem. Engng Sci.* **66** (14), 3204–3211.
ROGHAIR, I., VAN SINT ANNALAND, M. & KUIPERS, J.A.M. 2010 Drag force on bubbles in bubble swarms. In *Proceedings 7th International Conference on Computational Fluid Dynamics in the Minerals and Process Industry (CFD 2009)*, pp. 046ROG–1–046ROG–6. CSIRO.
ROGHAIR, I., VAN SINT ANNALAND, M. & KUIPERS, J.A.M. 2016 An improved Front-Tracking technique for the simulation of mass transfer in dense bubbly flows. *Chem. Engng Sci.* **152**, 351–369.

https://doi.org/10.1017/jfm.2026.11338 Published online by Cambridge University Press

SALIMI, S.Z., MUKHERJEE, A., PELANTI, M. & BRANDT, L. 2025 A low Mach number diffuse-interface model for multicomponent two-phase flows with phase change. *J. Comput. Phys.* **523**, 113683.
SANGANI, A.S. & DIDWANIA, A.K. 1993 Dynamic simulations of flows of bubbly liquids at large Reynolds numbers. *J. Fluid Mech.* **250**, 307–337.
SCARBOLO, L. & SOLDATI, A. 2013 Turbulence modulation across the interface of a large deformable drop. *J. Turbul.* **14** (11), 27–43.
SCHLICHTING, H. & GERSTEN, K. 2016 *Boundary-Layer Theory*. Springer.
SHU, S., VIDAL, D., BERTRAND, F. & CHAOUKI, J. 2019 Multiscale multiphase phenomena in bubble column reactors: a review. *Renew. Energy* **141**, 613–631.
SLATTERY, J.C. 1999 *Advanced Transport Phenomena*. Cambridge University Press.
SMEREKA, P. 1993 On the motion of bubbles in a periodic box. *J. Fluid Mech.* **254**, 79–112.
SMOLIANSKI, A., HAARIO, H. & LUUKKA, P. 2008 Numerical study of dynamics of single bubbles and bubble swarms. *Appl. Math. Model.* **32** (5), 641–659.
TANAKA, M. 2011 Numerical study on flow structures and heat transfer characteristics of turbulent bubbly upflow in a vertical channel. *Comput. Simul. Appl.* **20** (1), 119–142.
TRYGGVASON, G., LU, J. & BISWAS, S. 2006 Direct numerical simulations of bubbles in vertical channels. In *Proceedings of the ASME Fluids Engineering Division Summer Meeting*, vol. 1: Symposia, Parts A and B, pp. 513–517.
TRYGGVASON, G., MA, M. & LU, J. 2016 DNS–assisted modeling of bubbly flows in vertical channels. *Nucl. Sci. Engng* **184** (3), 312–320.
UNVERDI, S.O. & TRYGGVASON, G. 1992*a* Computations of multi-fluid flows. *Physica D* **60** (1–4), 70–83.
UNVERDI, S.O. & TRYGGVASON, G. 1992*b* A front-tracking method for viscous, incompressible, multi-fluid flows. *J. Comput. Phys.* **100** (1), 25–37.
VAN SINT ANNALAND, M., DEEN, N.G. & KUIPERS, J.A.M. 2005 Numerical simulation of gas bubbles behaviour using a three-dimensional volume of fluid method. *Chem. Engng Sci.* **60** (11), 2999–3011.
WEINER, A. & BOTHE, D. 2017 Advanced subgrid-scale modeling for convection-dominated species transport at fluid interfaces with application to mass transfer from rising bubbles. *J. Comput. Phys.* **347**, 261–289.
ZAREI, A., *et al.* 2025 Bubble injection for heat transfer enhancement: from physics to applications. *Phys. Rep.* **1112**, 1–117.
ZHANG, L., PENG, K., SHAO, X. & DENG, J. 2021 Direct numerical simulation of deformable rising bubbles at low Reynolds numbers. *Phys. Fluids* **33** (11), 113309.

https://doi.org/10.1017/jfm.2026.11338 Published online by Cambridge University Press